Investigating the vertical structure of sediment fluxes across an intertidal mudflat.

A thesis submitted in partial fulfilment

of the requirements for the degree

of

Master of Science (Research)

In Environmental Sciences

at

The University of Waikato

by

Toby Derek Beisly

THE UNIVERSITY OF
WAIKATO
Te Whare Wānanga o Waikato

2023

Abstract

Muddy coastal environments consisting of fine grained, cohesive sediment, are important systems for their provision of crucial ecosystem services. Such environments are governed by complex sediment transport patterns connecting the system to the wider coastal environment. To understand sediment transport it is necessary to measure suspended sediment concentrations and current velocities, from which, sediment fluxes can be estimated. Measurements of suspended sediment concentration (SSC) are typically carried out through the use of a variety of instruments, including, optical backscatter sensors or acoustic backscatter sensors; while acoustic Doppler velocimeters, electromagnetic current meters and acoustic Doppler current profilers are used to provide measurements of flow velocities.

To reliably estimate sediment flux, accurate vertical profiles of SSC and currents are required. Despite the need for profile information, typically flux calculations are based on observations from a single measurement location and exploited through the water column. However, the sensitivity of flux measurements to the vertical resolution (e.g., number of instruments) or to the method of extrapolation is rarely quantified.

This study elucidates the significant sensitivity of measurements to the instrument arrangement and technique used to extrapolate the data. Our results, taken in the field under real life conditions, indicate that single, or even double, vertical instrument arrangements are likely to have a large margin of error associated with any resulting flux estimates. However, a more even spread of instruments over the water column appears to give a more accurate estimate of flux. We find that under calm conditions (small waves) the Rouse SSC models provide a good estimate of SSC, while the velocity model, law of the wall, contains significant uncertainty in its velocity estimates. These results demonstrate the uncertainty associated with such dynamic environments, and as such, the need for robust measurement techniques and an understanding of the vertical structure of SSC and currents. Such understanding of sediment transport is crucial for making informed decisions around the management of intertidal muddy environments.

Acknowledgements

First and foremost, I would like to thank my supervisors; Julia Mullarney (University of Waikato) and Iain MacDonald (NIWA) for all their help throughout the project. Your encouragement, wealth of knowledge, and patience with me has been truly invaluable and made this research very rewarding.

I would also like to thank the Ministry of Business, Innovation and Employment (MBIE) for their financial support of the project for which I am very grateful. Their support has played a major role in enabling this research.

For all their help with the field and laboratory work I would like to give a big thank you to Ben Norris and Annette Rodgers. You were both always very willing to help out, answer questions and always did everything to a very high standard.

Thank you to Berengere Dejeans and Isabella Redder for their help with data processing and writing. In addition, I would like to thank Isabella for the data provided for this work, you've been a great thesis buddy to work alongside.

Finally, I would like to acknowledge all the friends and family who supported me over this time, thank you for all the encouragement, and an especially big thank you to my fiancé, Emily, for all your support.

Table of contents

List of figures

List of tables

Chapter 1: Introduction

1.1 Importance of sediment transport

Sediment transport in coastal regions influences morphology, water quality, ecosystem health, and navigability. Thus, a robust understanding of sediment movement is crucial for any coastal management and hazard mitigation strategies. Such strategies and numerical modelling of the movement and deposition of sediment all need to be underpinned and validated by accurate data. However, sediment transport is complex and influenced by many biophysical and geochemical processes, which can be spatially and temporally variable.

Due to this complexity, measurements need to be of a high quality and accuracy to allow subsequent monitoring or modelling to be reliable. Measurements are used to calibrate monitoring equipment and validate models, thus directly affecting model reliability. Data coverage is also important since measurements generally need to be extrapolated to cover a wider area. A greater degree of coverage will result in a better understanding of the spatial gradients at play. Small inaccuracies in data can be magnified when measurements or results are extrapolated across time or space.

Sediment input into coastal regions has been increasing significantly in New Zealand for over a century (Figure 1.1) (Jones et al., 2022). Increases can largely be attributed to land use change on steep hill country as a large proportion of native forest was cleared to make way for agriculture and forestry (Morrison et al., 2009). Forest clearing and resulting land use change can be linked to an increase in terrigenous sediment movement via landslides (Page & Trustrum, 1997; Trustrum et al., 1990) and thus the increased sediment delivery to aquatic systems (Glade, 2003). While the historic increase in sedimentation varies by location, Page & Trustrum (1997) found that sedimentation rates in a catchment increased by 8 to 17 times under agricultural use, compared to native forest. This dramatic increase in sediment availability has altered and continues to alter sediment transport patterns within the receiving water bodies. The associated changes in accretion and erosion have a wide range of impacts on coastal infrastructure, geomorphology, and ecology.

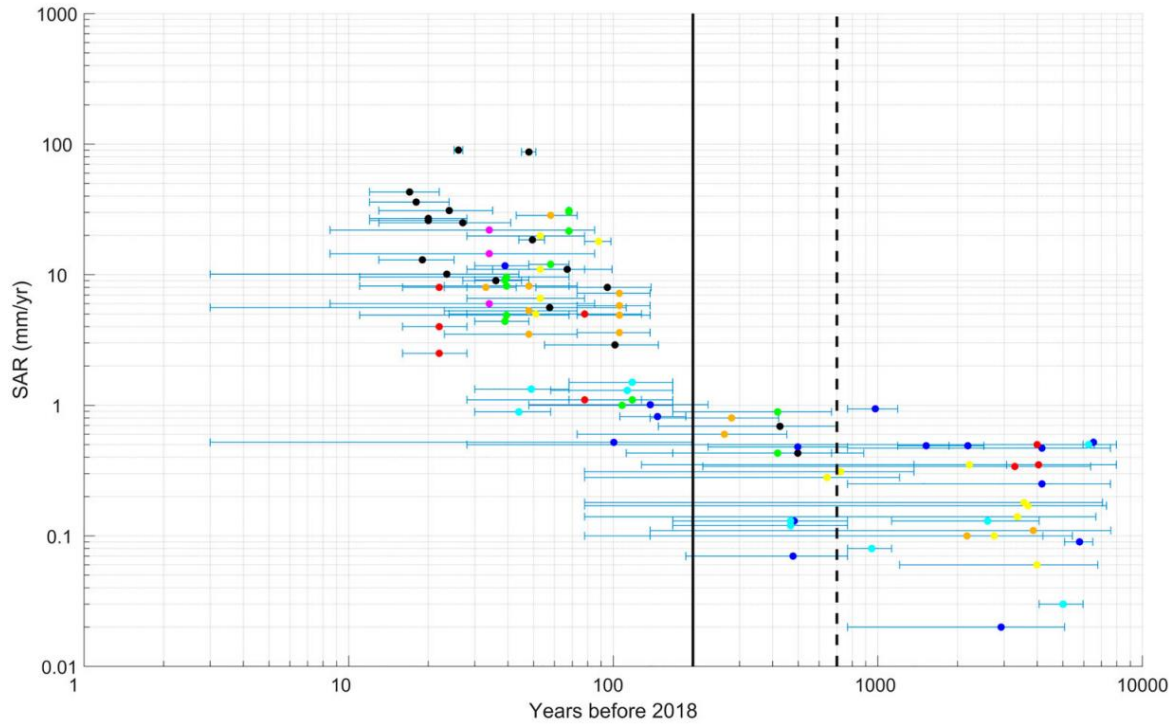

Figure 1.1: Sediment accumulation rates (SAR) from eight estuaries in the Waikato region, central North Island, New Zealand. The data of Polynesian settlement is denoted by the dashed line while European settlement is denoted by the solid line. Different estuaries are represented by different coloured points. From Jones et al. (2022).

Smothering and scouring resulting from sediment transport patterns are major stressors of marine ecosystems (Norkko et al., 2002; Shi et al., 2021), especially benthic ones. In both cases, sediment acts through a myriad of disturbance pathways to alter benthic communities in different ways depending on the nature of the sediment, environment, and affected ecosystem. In New Zealand, smothering as a result of sediment deposition or high suspended sediment concentration (SSC) is the most prominent stressor for these benthic communities owing to the country's high sedimentation rates (Thrush et al., 2004). Suspended sediment alters the light climate potentially blocking light from reaching primary producers, i.e., phytoplankton or seagrass, and reducing primary production. Additionally, suspended sediment alters available suspended food, especially for filter feeders feeding straight out of suspension (Thrush et al., 2004). Deposited sediments have the potential to smother flora and fauna or change the physical characteristics of the sediment (Thrush et al., 2004). For example, Rodil et al. (2011) found that in addition to reducing primary productivity, ecosystems treated with a thin (5 mm) layer of terrigenous sediment became phosphate-limited instead of nitrate-limited due to charged clay particles binding up phosphate. The sensitivity of these ecosystems to sediment input can be large,

with deposits as small as 1 mm having significant effects to ecological (Woodin et al., 2012) and physical functioning (Staudt et al., 2019).

In the opposite case scouring may occur, often due to a lack of sediment supply. As a result, nutrients and sediment that provide food and shelter for benthic organisms are stripped away (Hall, 2002). Reduced sediment supply can be induced anthropogenically by changes to flow regimes, e.g., dam construction on rivers feeding the area (Hall, 2002). Anthropogenic structures can also increase erosion by altering the wave regime, for example, Kim et al. (2022) found wave reflection off a nearby dike to be the main cause of increased erosion in their study site. In many cases, excess, or insufficient sediment supply will result in a reduction in ecosystem functioning. For example, in the case of sea grass, excess sedimentation results in light reduction and the subsequent smothering of seagrass communities (De Boer, 2007). However, sea grass, being highly light dependent (Dennison et al., 1993), can only survive above a certain depth, and as such, some sedimentation is required to increase bed height so that sea grass communities can keep up with increasing sea levels or expand their colonies into deeper waters (De Boer, 2007).

Both erosion and accretion can prove to be a significant hazard to coastal property and infrastructure. Ports, which are often located within estuaries, often require regular dredging of the estuary's inlet to maintain a navigable channel. As sediment loading to estuaries increases due to anthropogenic activities, the frequency of dredging also increases which represents a major cost for port authorities (Venancio et al., 2020). Just as anthropogenic alterations cause enhanced accretion in some areas, other areas are subject to erosional forces as a result of human activities. Alteration to coastlines (e.g., harbour construction, coastal defences, etc.) can create downdrift erosion as a result, often by trapping sediment that would otherwise be deposited downdrift (Williams et al., 2018). Such changes are not only limited to New Zealand. Owing to the high proportion of settlements located on coasts worldwide, the risk to property as coastlines retreat is significant. For example, Fitton et al. (2018) identified that in Scotland alone 3310 dwellings valued at around one billion dollars were exposed to coastal erosion. Coastal erosional issues are also predicted to be exacerbated by global eustatic sea level rise resulting from worldwide climate change (Zhang et al., 2004).

Furthermore, sediment transport is important for determining the fates of contaminants. Fine grained sediments tend to be "reactive" with many chemical components due to their large collective surface area and mineral structure (Nittrouer et al., 2017). This property

allows contaminating chemicals and compounds, anthropogenic in origin, to be absorbed by riverine sediments and transported to sediment sinks where these contaminants can accumulate or be resuspended and travel elsewhere (Nittrouer et al., 2017). Different types of contaminants can take a variety of transport pathways, and thus, have divergent fates, increasing the number potential sinks compared to being transported while dissolved in water.

Sediment loading of coastal environments is predicted to continue its increasing trend in New Zealand (Jones et al., 2022), although efforts are being made to counteract the increase, especially through developing better land use management strategies (Hughes et al., 2012). Changes to coastal environments, e.g., coastal hardening, dredging, etc., will have further effects on sediment movement regimes (Floerl et al., 2021). Furthermore, climate change is predicted to induce an additional increase in sediment loads, further altering sediment transport pathways (Suif et al., 2017; Wei et al., 2019). It should be noted that there is a high degree of uncertainty associated with predicting sediment load changes from climatic models. Predicting all these changes will be crucial for protecting estuarine environments, maintaining desired ecosystem services, and informing infrastructure decisions.

1.2 Sediment transport on intertidal mud flats

Tides, wind-driven waves, and sediment supply to the area are the primary drivers of SSC and currents in coastal areas, and thus constitute the primary controls on sediment transport. The majority of sediment constituting a mud flat is terrestrial in origin and delivered to the system via local rivers. However, for suspended sediment, a large portion of the suspended material moving to and from the flat will consist of resuspended sediment from the same mud flat or other intertidal flats in the same estuary, delta, etc. (Green & Coco, 2007; Green & MacDonald, 2001). The amount of sediment in suspension is also controlled by grain size. Larger particles have faster settling velocities, and as such, fall out of suspension at slower flows and require faster flows to be lifted off the bed and entrained in the water column. In contrast to large particles, fine particles can take a significant amount of time to settle after the flow speed reduces and is no longer able to support them. This process is known as settling lag.

The erosional force responsible for the majority of sediment resuspension is wind-driven waves (Hunt et al., 2015). Wind waves have much faster orbital velocities than their tidal counterparts, and as such, produce a greater bed stress force and promote erosion (Hunt et al., 2015). However, after being lifted off the bed, the sediment suspended is transported primarily by tidal currents. Net sediment movement (flux, expressed in units of g/L/s) into and away from the mud flat occurs as a result of tidal velocity asymmetry, in which the strength of incoming and outgoing tidal currents is not equal (Friedrichs & Aubrey, 1988; Hunt et al., 2017). As such, the tide will either be ebb-dominant, with stronger maximum offshore currents, or flood-dominant, with stronger maximum onshore currents.

Fluxes are further modified by spring and neap variations in the tidal range. While these variations alter the strength and coverage of tidal currents, the differences in water depths also affect how waves interact with the mud flat (Hunt et al., 2017). The manner in which spring/neap variations alter wave behaviour is further influenced by the fetch within the basin. For basins with sufficiently long fetches, the decay in wave orbital velocities associated with the deeper water depths at high tide, is mitigated by the longer fetches allowing for growth of larger waves. Consequently, wave orbital velocities can still reach the seafloor and bed shear stresses will be larger (than the tide only case). The relative balances between the different factors have been shown to vary between locations. While Hunt et al., (2017) found the reduced depth to be more important than fetch, and thus, erosion more prominent during neap tides, Fagherazzi et al., (2007) found the opposite to be true, with erosion being greater during spring tides. This result indicates that basin morphology among other factors also plays an integral role (Hunt et al., 2017).

The strength of wave and tidal energy relative to each other determines whether a system is tidally, or wave dominated. Typically, an intertidal flat will vary between times of tidal domination and times of wave domination depending on the active tidal cycle, wave climate, tidal range, etc. For example, Bassoullet et al. (2000) found their mud flat to be tidally dominated during spring tides, but wave dominated when tidal range reduced during neap tides. Various studies have correlated alternating periods of tidal and wave dominance with the erosional/depositional state of the flat. Both Andersen & Pejrup (2001) and Bassoullet et al., (2000) found the mud flats they were studying were accretional during periods of tidal domination and erosional while wave dominated, which is a trend for intertidal flats. The accretional or erosional state of a flat influences the morphology;

accreting flats tend to form a convex upwards cross shore profile, while eroding flats form a concave upward profile (Hunt et al., 2015; Friedrichs, 2011; Dyer, 1998).

Sediment supply dictates how much sediment is available in the system. Since intertidal flats are usually found in estuaries, the main source of sediment tends to be from rivers; however, some coastal sediment may also enter the estuary from outside on incoming tides. An increased sediment supply tends to promote deposition and expansion of intertidal flats, while a decrease in supply promotes erosion. The amount of terrestrial sediment supplied to a flat via rivers is dictated by the land use in those river catchments.

While mudflats represent environments of constant sediment flux, a quasi-equilibrium can be reached where erosion and deposition rates are equal over long time periods (monthly or longer), resulting in a stable morphological profile (Friedrichs & Aubrey, 1996; Lee & Mehta, 1997). Depending on environmental factors such as waves and tides, mudflats typically go through periods of alternating accretion and erosion during which flat morphology undergoes small changes. Despite these changes, if the flat has indeed reached an equilibrium state, the averaged morphology over a number of these alternating cycles will remain stable (Fan et al., 2006). The quasi-equilibrium profile of a mudflat is resistant to perturbation by periodic high magnitude events such as storms. Fan et al. (2006) found that a mudflat could recover from a large typhoon event in as little time as several tidal cycles. Long-term changes to a mudflats profile can occur as a result of a change in key forcing factors such as sediment supply or sea level.

Bed morphology is another characteristic influencing current speeds and SSC, potentially generating spatial variability, and thus, making it harder to get representative measurements. Whitehouse et al. (2000) concluded that bedforms have a significant effect on the spatial variation of flow and SSC when the water level is less than 3-5 times the local bedform height. Under these conditions, SSC tends to be greater above troughs (Whitehouse et al., 2000; O'Brien et al., 2000) and the effect is greater for larger bedforms. As such, large bedforms can greatly complicate measurements, especially when extrapolating over large areas.

1.3 Complications with fine grained cohesive sediments

Mud is made up of predominantly fine-grained sediments smaller than 62.5 μm, i.e., silts and clays (Wentworth, 1922). Of this category, a high proportion are clay minerals with

the remainder being silt or organic matter. Cohesion can occur due to electrochemical forces, biological bonding, or a combination of both (Mitchener & Torfs, 1996). Cohesive sediments are significantly more resistant to erosion (Grabowski et al., 2011) and have a number of parameters affecting erosion that make their erosional characteristics hard to model accurately. Organic component, biological processes, mineral composition, pore water composition and bed structure all play a role in dictating how and when these sediments will erode (Mitchener & Torfs, 1996). Cohesive sediments can also be challenging to measure accurately in suspension due to a process called flocculation. Flocs are formed as fine particles adhere to one another, often by large organic molecules, forming large irregular structures that have a comparatively low density due to gaps left within the structure (Eisma, 1986; Manning et al., 2010). The increase in mass compared to individual particles causes flocs to fall out of suspension more rapidly by significantly increasing settling velocity compared to the constituent particles (Manning et al., 2010). As a result, models that do not account for flocculation may incorrectly predict settling locations of particles.

In the field, measuring the size of flocs is challenging, although can be done with specialised equipment, for example, floc cameras; however, this technique is limited to smaller concentrations (e.g., ~0.35 g/L, MacDonald & Mullarney, 2015) and only provides a two-dimensional estimation of floc size (MacDonald & Mullarney, 2015). Similarly, in some environments, researchers have successfully obtained particle size distributions with laser diffraction instruments such as the LISST (Laser In-Situ Scattering and Transmissometry); however, these instruments cannot accurately resolve particle size distributions in regions with strong salinity gradients (Styles, 2006).

In addition, when flocs are in suspension, it is not possible to obtain a water column profile of SSC which would be achieved using acoustic backscatter sensors (ABS), a suite of instrumentation that offers much higher spatial resolution than optical backscatter sensors (OBS) (Thorne & Hurther, 2014; Thorne et al., 1991). ABS estimates of SSC rely on a theoretical framework to describe the interaction of the sound wave with the particle being measured. These estimates have been achieved for irregularly shaped sand sized particles and smaller spherical particles (Thorne et al., 2014); however, it is significantly more difficult to describe the scattering properties of complex floc structures. As such, flocculation acts to confound SSC estimates derived from ABS measurements (Thorne et al., 2014).

1.4 Estimating sediment fluxes

The amount of sediment transported through a unit area per unit time is the sediment flux. The most common way to measure sediment fluxes therefore is to use co-located velocity and concentration measurements. Velocities are typically measured either at a fixed point using an Acoustic Doppler Velocimeter (ADV) (Andersen & Pejrup, 2001; MacVean & Lacy, 2014; Shi et al., 2016) or electromagnetic current meter (EMCM) (Bassoullet et al., 2000; Christie et al., 1999; Dyer et al., 2000), or along a profile using an Acoustic Doppler Current Profiler (ADCP) (Nowacki & Ogston, 2013). Concentrations are measured with either OBS (optical backscatter sensor) (Bassoullet et al., 2000; Deloffre et al., 2005; Nowacki & Ogston, 2013) or ABS (acoustic backscatter sensor). These instruments provide output in volts or arbitrary units, and thus need to be calibrated to provide SSCs. A site and time-specific calibration curve relating OBS output to actual SSC can be constructed through laboratory measurements using sediment representative of that from the field site, which is typically obtained from surface grab samples (Nowacki & Ogston, 2013). Alternatively, water samples may be taken directly from the field to calibrate the OBS (Andersen & Pejrup, 2001).

When estimating sediment fluxes in this manner, there are usually some assumptions that need to be made, and these assumptions may affect the potential error of estimates. A major, commonly applied assumption is that velocity and SSC are uniform throughout depth, i.e., the vertical water column is well mixed. In this case, only one pair of OBS and ADV instruments are deployed to measure at a single depth and the values applied over the whole water column (Andersen & Pejrup, 2001; Nowacki & Ogston, 2013). When measuring at a single height, instruments typically need to be deployed close to the bed in order to capture as much of the tidal cycle as possible. For example, Andersen & Pejrup (2001) deployed instruments on two occasions, at 0.2 and 0.5 m above the bed where maximum water depths per tide were around 1.25 m. SSCs throughout the water column typically follow the Rouse profile (Figure 1.2) (Rouse, 1937). As such, SSC is larger near the bed and extrapolating from an instrument near the bed may result in overestimating the SSC throughout the water column. Conversely, an instrument located higher in the water column will miss a portion of the tidal cycle and low water transport, which is likely significant, thus underestimating fluxes and/or SSC values. Some researchers have deployed more (usually two) OBS and/or ADV's in the vertical to try to ascertain

sediment flux values. Additionally, instead of assuming the same measurements across the water column, some researchers extrapolate their data using a model profile. For example, Bassoullet et al. (2000) measured velocity with an ADV at a single height and assumed a logarithmic velocity profile throughout the water column. To obtain SSC, two OBS were used at different heights and the water column was effectively split into two layers around each OBS, within which, SSC was assumed to be uniform. Resulting time integrated flux reached around 20,000 kg/m.

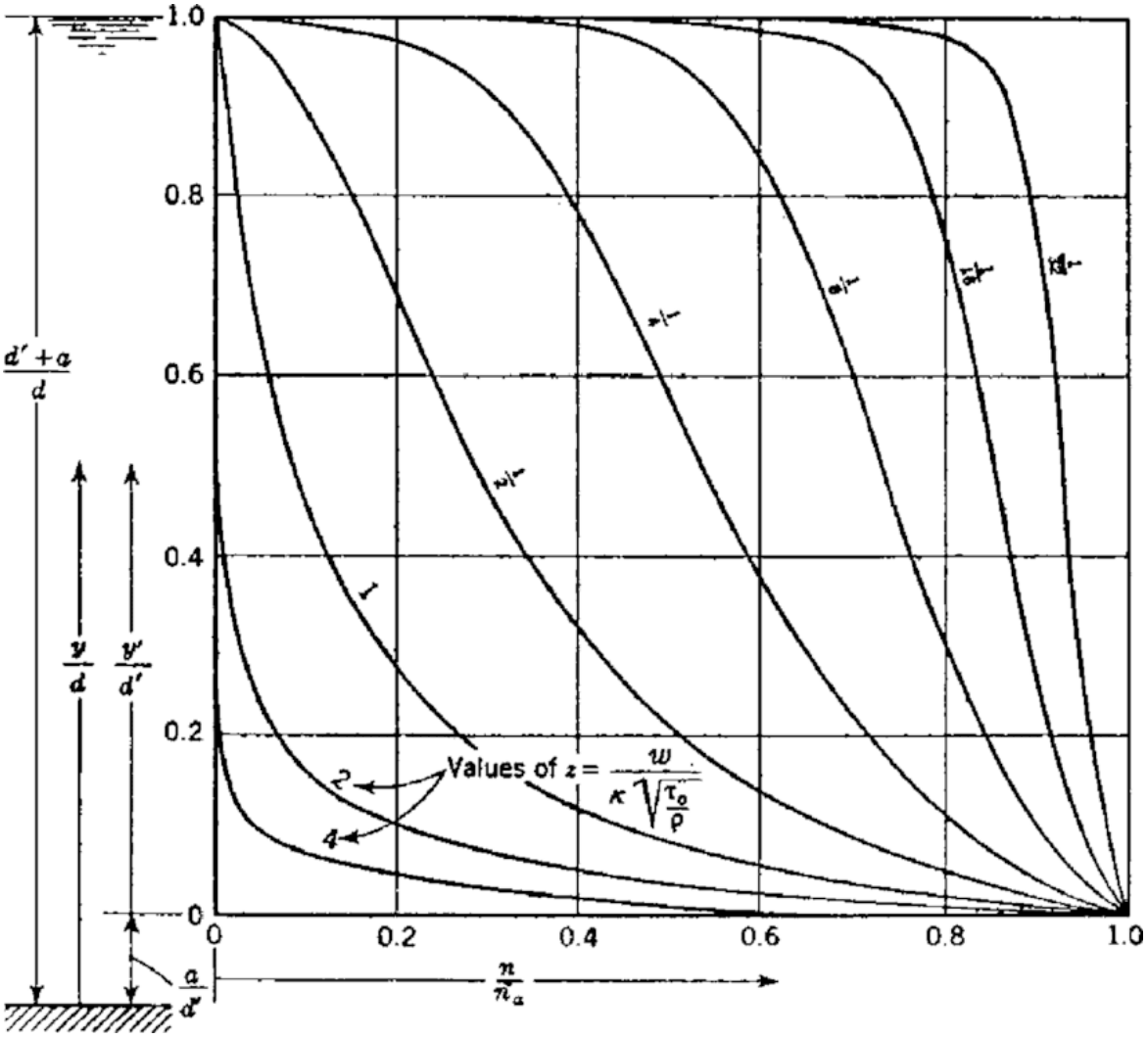

Figure 1.2: Dimensionless plot of rouse profiles with suspended particle concentration (n) plotted against depth (y) for different Rouse numbers (z), where w = particle fall velocity; T0 = boundary shear stress, p = fluid density, and k = the von Kármán constant. From Rouse (1937).

1.5 Knowledge gaps and thesis aims

The use of co-located SSC and velocity measurements to estimate sediment fluxes is widespread throughout coastal oceanographic research (Nowacki & Ogston, 2013; Dyer et al., 2000). However, these studies do little to address the potential error derived from extrapolating SSC and/or velocity over the water column from few data points. As such, there is a lack of studies investigating the sensitivity of flux measurements to the method of data collections, i.e., deployment height above bed, number of instruments, etc.

This study aims to address this knowledge gap by exploring the sensitivity of fluxes to the vertical structure of velocity and SSC within the water column, and as such, answer the question:

How sensitive are estimates of sediment flux collected in the field to the arrangement and quantity of deployed instruments?

Results from this study will quantify the degree of error that may be associated with certain assumptions.

1.6 Thesis Structure

This thesis is written in an extended paper style. The structure is as follows:

- Chapter 1 introduces the topic, discussing relevant processes and research.
- Chapter 2 describes the field experiment site, methodology, and data processing methods.
- Results are presented in Chapter 3 with particular emphasis on sediment fluxes.
- In Chapter 4 findings are discussed along with their implications.
- Finally, conclusions are presented within Chapter 5, along with suggestions for future work.

Chapter 2: Field Experiments and Data Processing

2.1 Study Site

A field experiment was conducted on the southern intertidal flats of the Firth of Thames, a mesotidal estuary on the North Island of New Zealand (Figure 2.1). The Firth has an area of ~800 km^2 with ~70 km^2 of intertidal flats, and is fed by two main rivers, the Waihou and Piako (Swales et al., 2015). The rivers have a combined catchment area of 3,442 km^2 and supply the area with 160 000 t yr^{-1} and 30 000 t yr^{-1} of suspended sediment, respectively (Hicks et al., 2011). Healy (2002) found that riverine sediment input into the estuary tends to get trapped by circulation in the estuary driven by counter-directional winds. The Firth is meso-tidal with semi-diurnal tides (mean tidal range of 2.55 m) (Swales et al., 2015).

The mudflats that are located on the southern end of the Firth are composed of fine-grained cohesive sediments (median grainsize of 9.5 μm, Figure 2.2). The sediment of the flats is mostly terrigenous, originating from eroded volcanic deposits upstream. A large proportion of the suspended sediment input into the estuary is volcanic glass (roughly 50%) which breaks down into smectite via a diagenetic process (Naish et al., 1993). Smectite is a phyllosilicate clay mineral and makes up a large portion of the mud deposits found in the Firth (Naish et al., 1993). The southern end of the mudflat is characterised by a ~1 km wide mangrove forest (composed of *Avicennia marina*) which has expanded rapidly since the 1950s (Horstman et al., 2018).

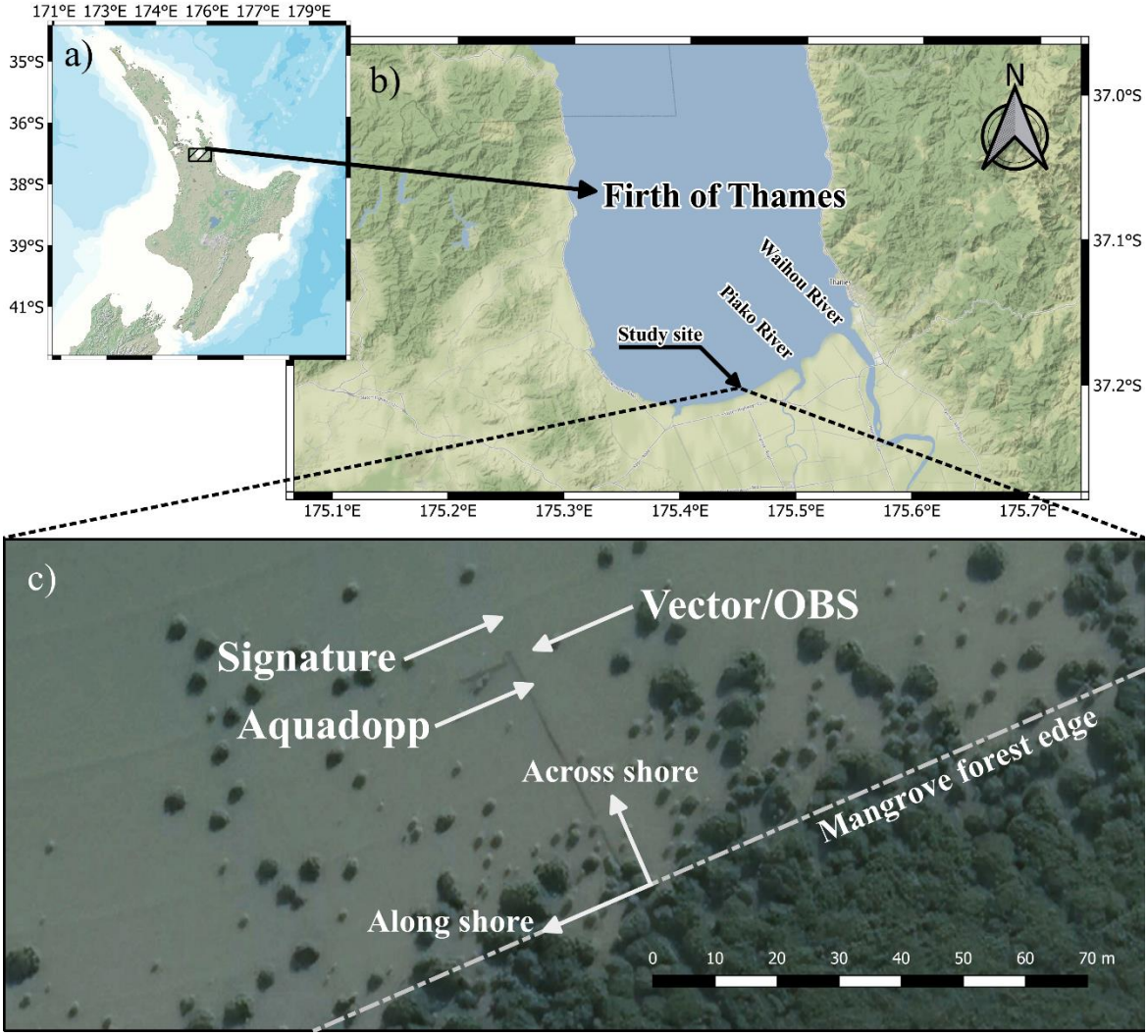

Figure 2.1: North Island of NZ with the Firth of Thames outlined (a). The location of the study site and major rivers outflowing into the firth (b). Google satellite imagery of the study site from 30/5/2022 (c). The directions of rotated alongshore and across shore velocities are indicated.

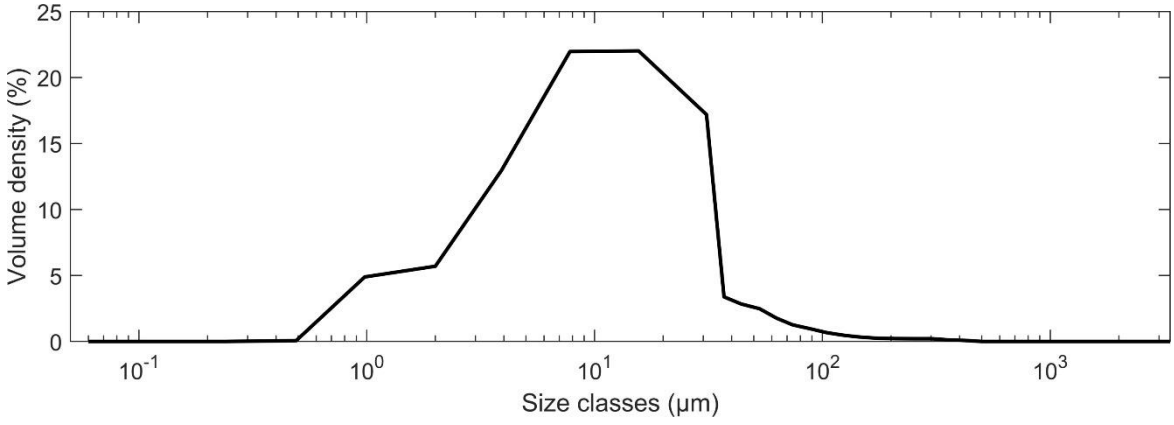

Figure 2.2: Grain size distribution by volume density percentage, plotted on a log scale.

2.2 Experimental Setup

An array of instruments was deployed over 6 tidal periods (6/11/2021 – 9/11/2021) referred to throughout the text as tides 1-6 in order of earliest to latest. The instruments were deployed ~50 m seaward of the fringe of the mangrove forest (Figure 2.1) that extends approximately 800 m from the shore. The primary frames (Figure 2.3) consisted of four Acoustic Doppler Velocimeters (ADVs, Nortek Vectors) deployed to measure three components of velocity at heights of 0.09, 0.20, 0.40 and 0.76 m above the bed with a sampling rate of 16 Hz. Additionally, temperature and pressure were recorded at the height of the instrument housing (Table 2.1). An optical backscatter sensor (OBS) was connected to each ADV to measure optical backscatter at 16 Hz at the same height as the velocity measurement. Tubes for water sampling were also located on the instrument frame at the same height of each corresponding OBS. Additionally, one tube was secured 1-2 cm above the bed to provide near-bed water samples. In-situ water samples were collected on site during tides 4 and 6. Water samples were taken by pumping water through each individual tube sequentially from lowest to highest above the bed, starting from when each tube intake was submerged. Once all tube intakes were submerged, each full set of samples was taken at approximately 15-20 minute intervals.

Two acoustic Doppler current profilers (ADCPs) were deployed, seaward and landward, at 6.5 and 5.6 m, respectively, from the Vector/OBS frames, to measure a profile of velocities through the full water column. The seaward most instrument was a Nortek Signature 1000, sampling continuously at 4 Hz with a vertical resolution (rangebins) of 0.2 m and a blanking distance of 0.3 m. The centre beam was also set to operate in echosounder mode with a vertical resolution of 3 mm and a blanking distance of 0.115. The landward instrument was a 2 MHz Nortek Aquadopp sampling at 1 Hz with a blanking distance of 0.2 m and a vertical resolution of 0.1 m. An OBS was also connected to the Aquadopp sampling at 0.2 m above the bed. Instrument settings are summarised in Table 2.1.

As part of a larger experiment, two Aquascat acoustic backscatter sensors, (ABS) were also deployed. One was on a floating frame with 4 downward-facing transducers, one was mounted at ~1m from the Vector frame with 4 upward-looking transducers (of frequencies 1, 2, 4, and 5 MHz) sampling at 16Hz with 10 mm along-range resolution. Data from the upward looking system underwent quality control as part of another MSc project (Redder, 2023), to remove data from above the water surface and average data into 10-minute

bursts. Profiles of SSC inverted from the quality-controlled backscatter data were provided by Redder (2023) for use here.

To minimise disturbances to the substrate during deployments, the main frame was deployed using a cantilevered platform constructed in 2016 (Figure 2.4). The cantilevered platform could extend above the substrate allowing instruments to be deployed with minimal disturbance. Additionally, the cantilevered platform could be retracted to eliminate any effects on flow characteristics during the experiment. Instruments were deployed a day prior to recording to allow for disturbances to settle.

Meteorological data (wind speed, direction, and atmospheric pressure) was collected from a weather station 1 km inland measuring at a height of 10 m.

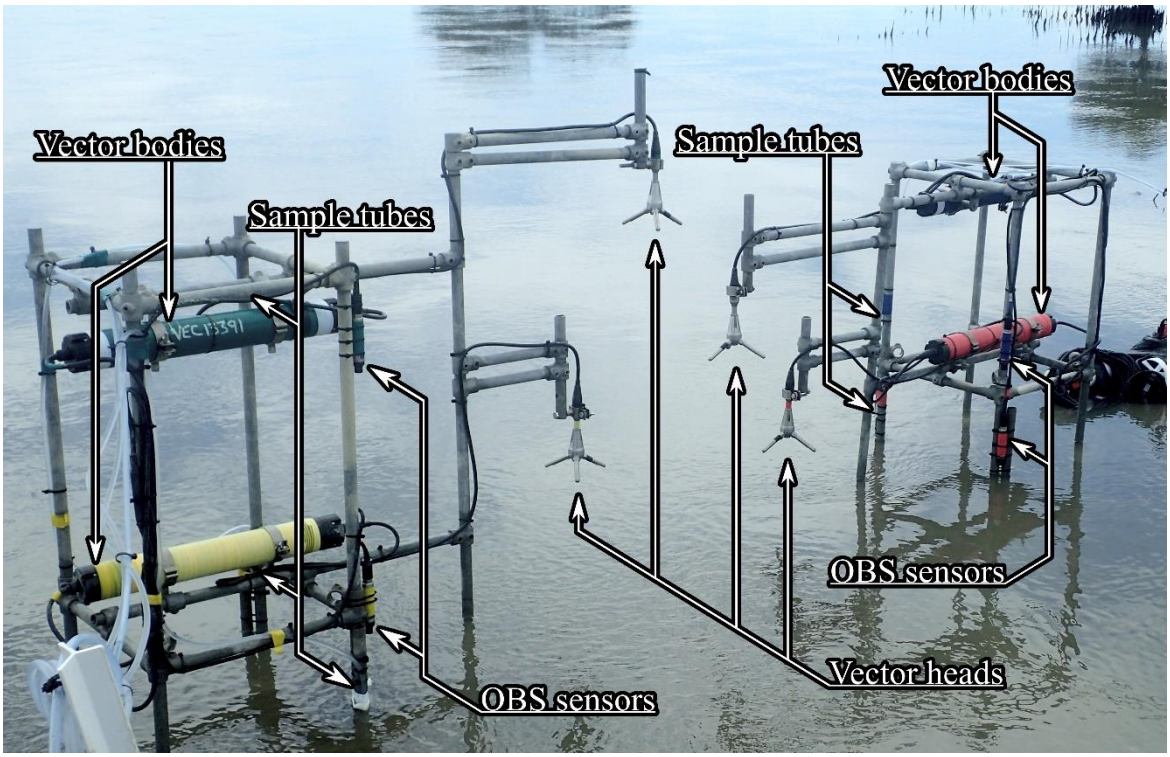

Figure 2.3: Setup of acoustic current velocimeters (Vectors) and optical backscatter sensors (OBS) with four of each deployed at 4 unique heights above the bed. The instrument frames are constructed to minimise disturbance to flow near instruments and have large feet to prevent sinking in the soft substrate. Tubes for water samples to be pumped through were attached at the 4 instrument heights as well as one near the bed.

Table 2.1: Overview of instrument location, recorded variables, and configuration information. HAB = height above bed in metres.

Location	Instrument	Variable measured	Configuration
Loc 1	Signature	Velocity Temperature Pressure Acoustic backscatter	4 Hz, continuous Outer beams: Blanking distance = 0.3 m Vertical resolution = 0.2 m Centre beam: Blanking distance = 0.115 m Vertical resolution = 0.3 m
Loc 2	Vector*4	Velocity Temperature Pressure Current direction	16 Hz, continuous HAB (Vector head measurement point) = 0.09, 0.20, 0.40, 0.76 HAB (body measuring temperature and pressure) = 0.39, 0.32, 0.80, 0.81
	OBS*4	Optical backscatter	HAB = 0.09, 0.20, 0.40, 0.76 Analogue input to Vector at respective HAB
	Sample Tube*4	SSC	HAB = 0.09, 0.20, 0.40, 0.76
Loc 3	Aquadopp	Velocity Temperature Pressure Acoustic backscatter	1 Hz, continuous HAB = 0.08 Blanking distance = 0.2 m Vertical resolution = 0.1 m
	OBS	Optical backscatter	HAB = 0.20 Analogue input to Aquadopp

Figure 2.4: Cantilevered platform extending out perpendicular to the shore normal orientated boardwalk. Instruments were deployed from the platform to minimise disturbance to the substrate. During measurement the platform was retracted to prevent any disturbances to flow.

2.3 Data processing and quality control

To ensure data was of a high quality and accuracy, various steps were taken to eliminate poor quality data. Firstly, data at the start and end of the record was removed, as well as data in-between tides when the instruments were out of the water. Vector data with a signal to noise ratio (SNR) below 15 or correlation (COR) below 70 was deemed of poor quality and removed. Any short data gaps were filled using linear interpolation. Atmospheric pressure fluctuations were removed from the pressure sensor data using data from the weather station. Pressure was subsequently converted to depth using the Gibbs-SeaWater toolbox (McDougall & Barker, 2011). All raw data measured by the various instruments was averaged over 10 minutes to form burst-average quantities. Velocities were rotated by 23.5° into across-shore (v), along-shore (u) (Figure 2.1), and vertical components with negative across-shore values corresponding to onshore velocity. Unless explicitly stated otherwise, all data presented herein are burst-averaged values.

2.3.1 Calibration of OBS sensors

The OBS sensors were calibrated to obtain estimates of suspended sediment concentrations (SSC). For the OBS sensors associated with the ADVs, both a calibration using in-situ water samples and a laboratory calibration were undertaken. For the OBS instrument associated with the landward ADCP (Aquadopp), only a laboratory calibration was completed. For all instruments SSC estimates were obtained using the linear relationship:

$$SSC = G\beta + O, \qquad (1)$$

where β is the OBS response in counts, G is the sensor gain (in units of g/L/count), and O is the sensor offset of g/L.

To calibrate the instruments in the laboratory sediment, samples were taken from surficial bed sediments near the instruments. Due to the greater sensitivity of the OBS to fine grain particles, the sediment was wet sieved to remove any particles larger than 63µm. The resulting slurry of fine sediment was used to calibrate the OBS.

A ~41 litre steel tank (Figure 2.5) was used for the calibrations with 3 pumps to prevent the sediment from settling out. Sediment was gradually added to cover the range of voltages/counts observed in the field with 12 concentrations used. A water sample was collected from each stage.

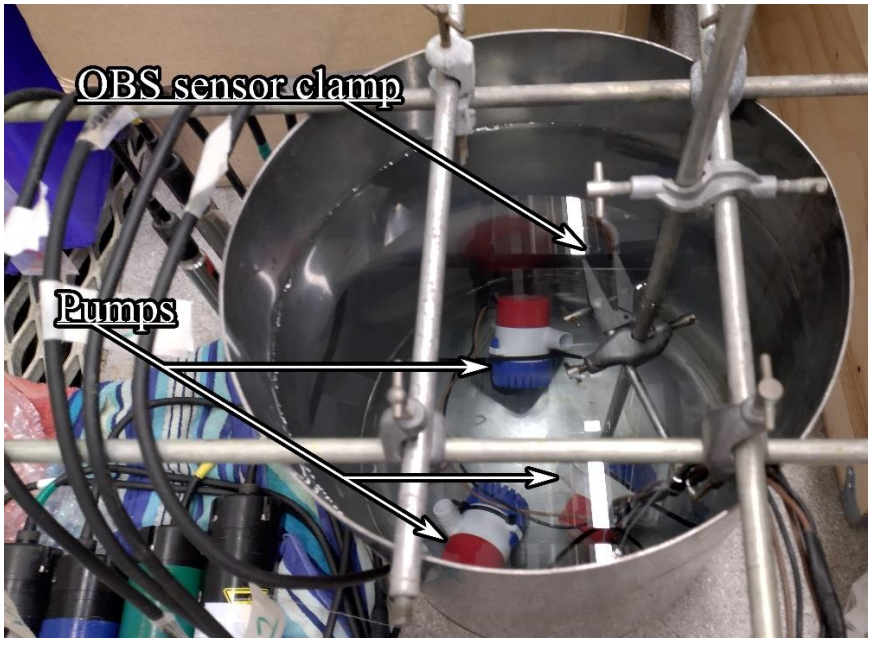

Figure 2.5: Steel tank used for laboratory calibrations with three water pumps to circulate water and maintain a homogenous SSC.

Water samples from the field and laboratory calibrations were filtered through Whatman glass microfiber filters (GF/C diameter 47 mm) to ascertain SSC values. The filters were dried at 105°C overnight prior to weighing and filtering the water samples. Post filtering, the filters were then dried for at least 12 hrs at 105°C to remove any moisture from the sediment and weighed again. SSC was calculated from the weights and sample volume as mass/volume (g/L). To remove organics, the filters were heated in a furnace for 4 hrs at 550°C and weighed again to provide an estimate of organic content.

2.3.2 Wave Statistics

Relevant wave statistics were calculated using pressure data from the Vector body at 0.39 m above the bed, and the methodology described in Green & Coco (2007), which is summarised here. Mean spectral period (*T*), significant wave height (*Hs*) and significant orbital speed at bed (U_{sigb}) were calculated following Green & Coco (2007). Mean spectral period was calculated as:

$$T = m_0/m_1 \,, \qquad (2)$$

where m_n is the *n*th moment of the power spectral density of the water depth. m_n was calculated as:

$$m_n = \int_{\frac{1}{30}s^{-1}}^{1\,s^{-1}} f^n S_h(f) df \,, \qquad (3)$$

where f is frequency and $S_h(f)$ is the power spectrum of *h(t)*. The integration limits correspond to the frequencies of interest, those pertaining to gravity-waves. Significant wave height H_{sig} was calculated as:

$$H_{sig} = 4h_{SD}\frac{\cosh(kh)}{\cosh[k(z^*+h)]} \,, \qquad (4)$$

where h_{SD} is the standard deviation of *h(t)*, *z** is the depth of the pressure sensor below the mean water level, and *k* is the wave number (which is a function of wave period and water depth).

Finally, significant orbital speed at the bed (U_{sigb}) was calculated as:

$$U_{sigb} = \frac{4\pi h_{SD}\cosh(kh)}{T\cosh[k(z^*+h)]\sinh(kh)} \,, \qquad (5)$$

From equations 3 and 4 we see that both *Hs* and U_{sigb} depend on the wave number (*k*), which is given by the dispersion relationship, which reads;

$$w^2 = gk \tanh(kh), \quad (6)$$

where $w = 2\pi/T$. Given the nonlinearity of Equation 6, a solution for k was obtained using the bi-section method (Wheatley, 2004).

2.3.3 Velocity modelling

The benthic boundary layer is the portion of the water column in which flow is directly influenced by the presence of the sediment-water interface, i.e., due to friction. The law of the wall (otherwise known as the logarithmic law) can be applied to flow velocity in order to estimate velocity at a certain distance from a no slip boundary condition. The law of the wall, friction velocity ($\bar{\upsilon}^*$), bed roughness (z_0), and the drag coefficient (C_D) were estimated from the law of the wall, using the method described in Green et al. (1998). Friction velocity $\bar{\upsilon}^* = K/M$ was calculated using the slope of the best fit line (M) and von Karman's constant ($K = 0.41$). Hydraulic roughness was calculated as $z_0 = e^B$, where B is the intercept of the best fit line. The velocity profile predicted by the law of the wall is given by:

$$\bar{\upsilon}_z = \left(\frac{\bar{\upsilon}^*}{K}\right) ln\left(\frac{z}{z_0}\right), \quad (7)$$

where $\bar{\upsilon}_z$ is the mean current velocity at elevation z above the bed. The drag coefficient (C_D) was calculated from z_0 as:

$$C_D = \left[\frac{K}{ln\,(1/z_0)}\right]. \quad (8)$$

2.3.4 Sediment fluxes

To determine sediment transport in the onshore and offshore directions, sediment fluxes (Q) were calculated from SSC and velocity data as:

$$Q = \int_0^h c(z)\, v(z)\, d(z)\,, \qquad (9)$$

where *c(z)* is the SSC profile and *v(z)* is the velocity profile perpendicular to the shoreline (which is approximately in the N–S direction). A resulting positive flux represents movement of sediment seaward while a negative flux indicates shoreward sediment movement.

For flux estimates, different approaches to defining the vertical profiles were explored, in order to investigate the sensitivity of said estimates. As such, a variety of different extrapolations were applied to the velocity and SSC profiles prior to calculating flux. These extrapolations are detailed in Figure 2.6 as Ex1, Ex2, etc. Ex1 best represents the expected SSC and velocity values, and as such, represents the reference. Velocity is extrapolated straight upward from the highest data point to the water surface and from the lowest data point to 0 at the bed. This represents the no slip boundary condition in which the velocity is equal to zero at the bed. SSC is extrapolated straight up and down from the highest and lowest data point, respectively. As the best estimate of the SSC and velocity profiles, any future flux values have been calculated using Ex1, in combination with, measured SSC and velocity data, unless explicitly stated otherwise.

For Ex2 and Ex3, only the upper (i.e., to the water surface) or lower (i.e., to the bed) portion of the Ex1 extrapolation was applied. The upper portion was applied to Ex2 and the lower portion to Ex3 (Figure 2.6). This was done for both SSC and velocity. All remaining extrapolations (Ex4 to Ex10) used the same method as Ex1 to extrapolate data upward to the surface, and downward to the bed.

Ex4 to Ex7 were calculated from profiles in which Velocity and SSC data from only a subsect of the vertical array of instruments was used. For Ex4, only SSC and velocity data from the instrument at 0.09 m above the bed was used in the SSC and velocity profiles. For Ex5, data from the instruments at 0.09 and 0.2 m was used in the profiles. For Ex6, data from the instruments at 0.09 and 0.4 m was used in the profiles. And for Ex7, data from the instruments at 0.2 and 0.4 m was used in the profiles.

Ex8 to Ex10 were calculated using SSC data from 1-2 instruments, in combination with, velocity data from all 4 instruments. The SSC data used for Ex8 to Ex10 is equivalent to that used in Ex4 to Ex6, respectively.

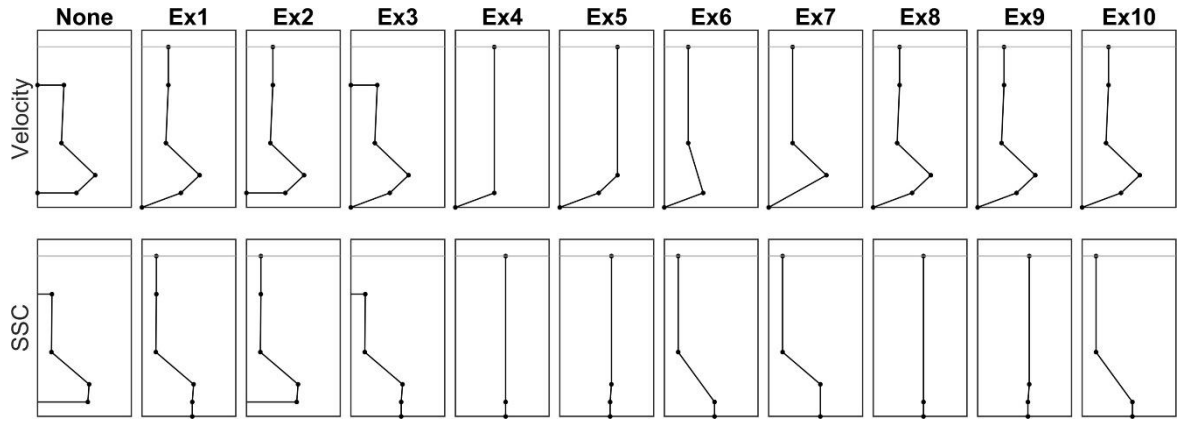

Figure 2.6: Schematic diagram of extrapolation methods used to extrapolate SSC and velocity. Profiles are examples of actual velocity and SSC profiles.

Three models were fitted to the SSC profile. In model one, linear diffusivity is assumed across the water column *C(z)*. Model one was calculated as:

$$C(z) = C_R \left(\frac{z}{z_a}\right)^{-W_s/KU_*}, \qquad (10)$$

where C_R is the reference concentration, z_a is a reference height (0.09 m), W_s is settling velocity, K is the Karman constant of 0.41, and U_* is friction velocity. Model two assumes constant diffusivity calculated as:

$$C(z) = C_R exp\left(\frac{-W_s}{K_o} z\right), \qquad (11)$$

where K_o is diffusivity. Model three assumes parabolic diffusivity calculated as:

$$C(z) = C_R \left(\frac{z}{h-z} \ \frac{h-z_a}{z_a}\right), \qquad (12)$$

where h is water depth.

Chapter 3: Results

3.1 Environmental conditions

Maximum water depth ranged from 0.97 to 1.19 m across the 6 tides. In general, current velocities were more flood oriented at lower depths and more ebb oriented higher in the water column (Figure 3.1). Typically, velocities were less than 0.1 m/s. For the flood tide, the current direction was typically around 200°, while for the ebb tide, the direction was typically around 340°.

The time-series of wind speed and direction is shown in figures 3.2 (a) and 3.2 (b), respectively. The mean wind speed over the deployment period was 2.5 m/s. The maximum wind speed during the same period blew from NW at 6.3 m/s. In general, conditions were calm, with significant wave heights of under 0.1 m, except for the first tide, during which they reached as high as 0.24 m. The maximum wave heights coincided with a northerly wind direction (approximately 0°). The maximum wave height for each tide was 0.24, 0.05, 0.1, 0.05, 0.1, and 0.07 m, respectively. Similarly, the significant orbital velocities at the bed reached 0.25 m/s during the first tide but remained less than 0.15 m/s for the remainder of the experiment.

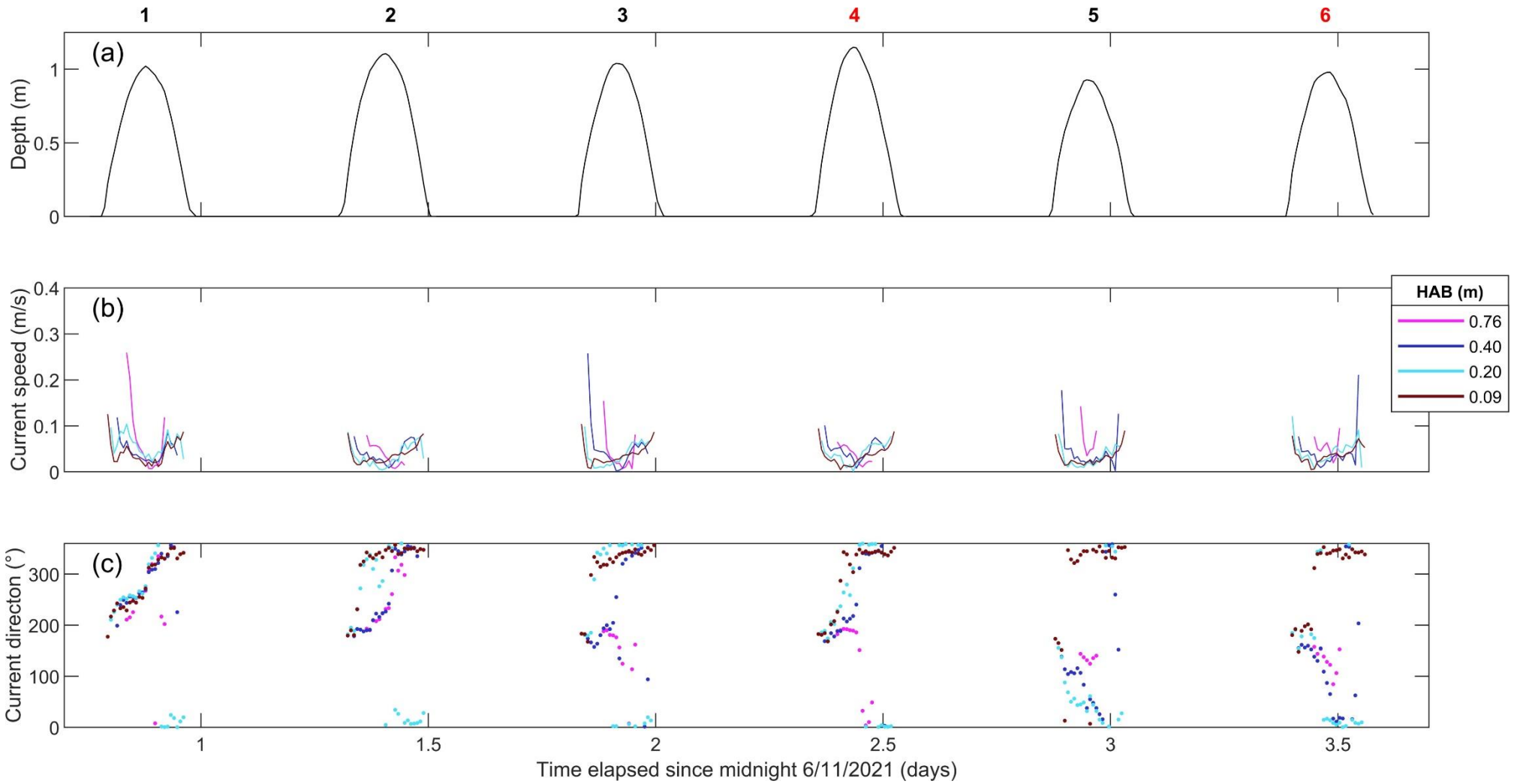

Figure 3.1: Environmental conditions over the deployment period. Depth in metres from the Aquadopp pressure sensor (a), current speed (b), and current direction in degrees (c) from the Vectors, where 360/0° represents offshore flow, and 180° represents onshore flow. The Numbers 1-6 represent the tide number as referred to throughout the text. Tides during which water samples were taken are denoted with a red tide number.

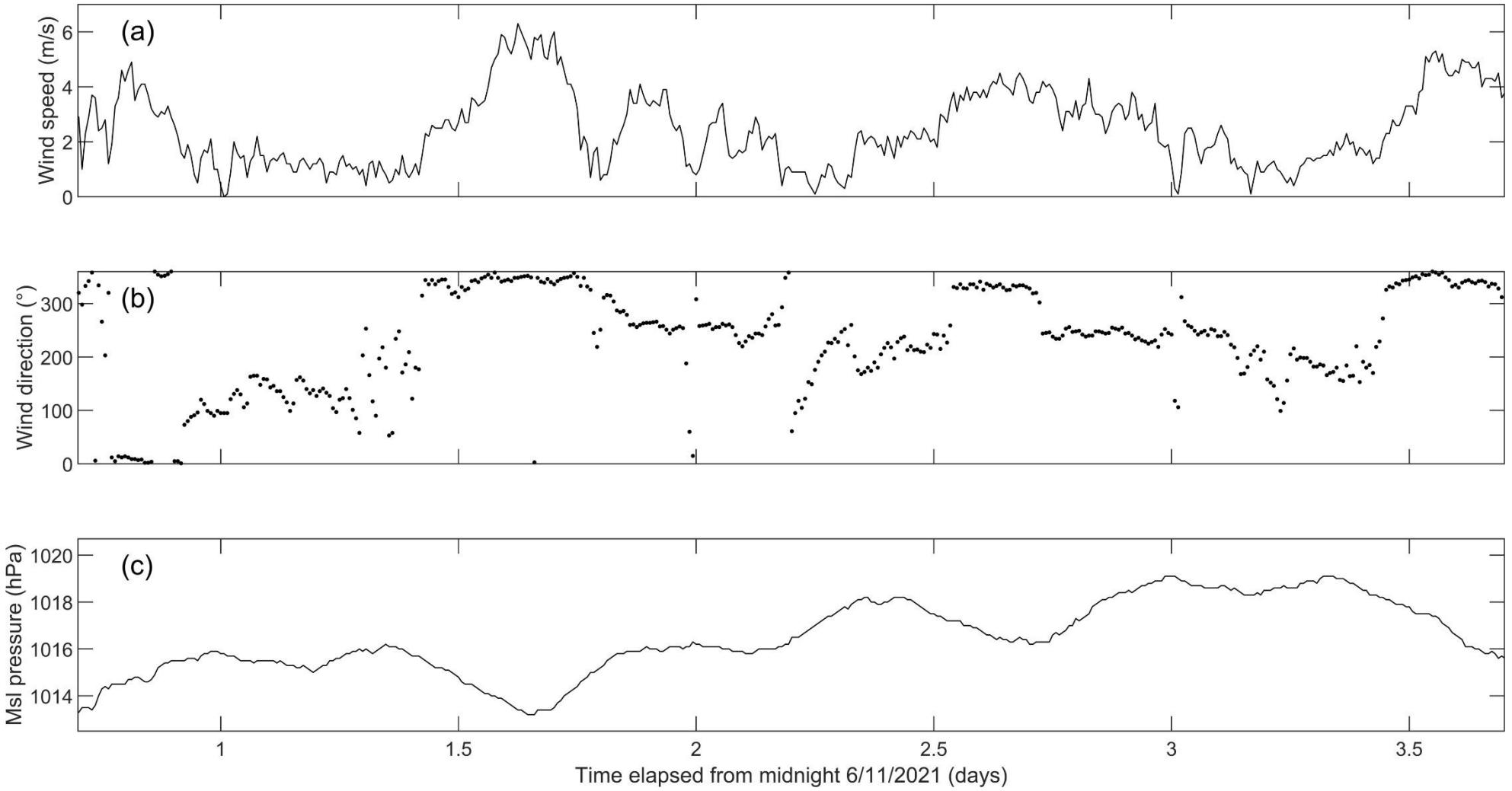

Figure 3.2: Weather data for the Firth of Thames during the deployment period. Wind speed in meters per second (a), Wind direction in degrees (b) where 0/360 degrees represents northerly winds, and pressure in msl (c) are presented.

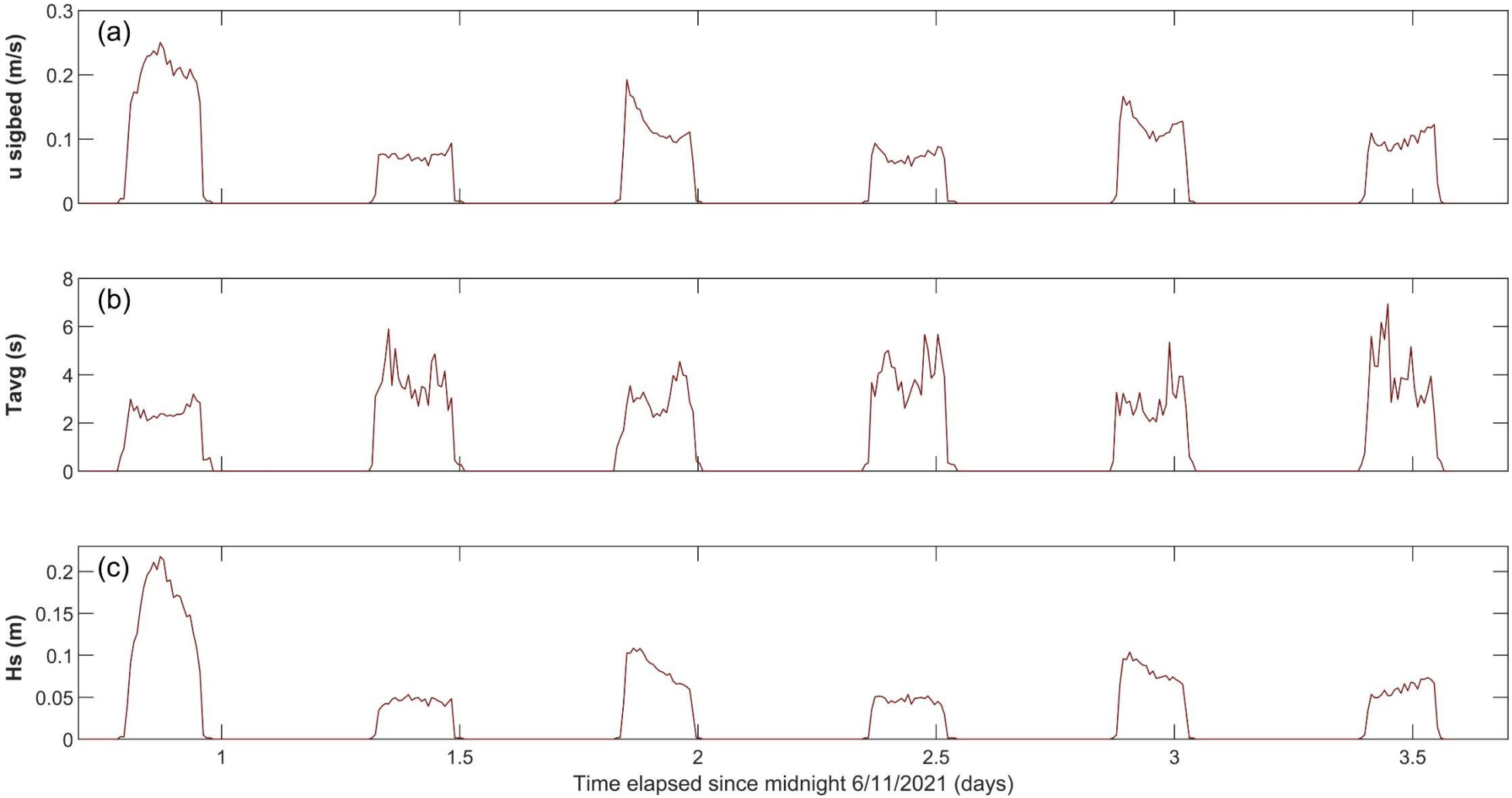

Figure 3.3: Wave statistics calculated the Vector body pressure sensor located at 0.39 m above the bed. Significant orbital velocities at the bed (a), mean wave period (b), and significant wave height (c) are plotted as time series.

3.2 OBS Calibrations

SSC data from the laboratory and field water samples was fitted linearly to the associated OBS response (Figure 3.4). The laboratory calibration covered SSC values ranging from 0.004 to 2.35 g/L. While the field calibration ranges varied per instrument, a range of 0.006 to 0.98 g/L of SSCs were covered. The coefficient of determination (R^2) values for the fits were generally slightly better when calibrating data with a lower gain setting. Calibration fits from laboratory data had relatively high R^2 values between 0.97 and 0.99 (Table 3.1). Fits using field derived data had significantly lower R^2 values. While the instruments at heights 0.09 and 0.2 m had acceptable values of $R^2 > 0.83$, the instruments at heights 0.4 and 0.76 m had very low R^2 values, between -0.2 and 0.66 (Table 3.1).

Table 3.2 displays the difference between water sample SSC and OBS SSC derived from the laboratory calibration. Differences range significantly from < 1 to 380 %. Two groups of large differences were observed for the instruments at 0.4 and 0.76 m above the bed toward the end of sampling during tide 6. In general, differences for the instruments at 0.09 and 0.2 m above the bed were significantly lower than the other two instruments. It should be noted that the field calibrated SSC showed similar differences with the water samples (typically ±15 % of the laboratory differences).

Each OBS instrument output data at two gain settings, one higher and one lower. While the majority of data fell within the range of the lower gain setting (higher sensitivity), some data exceeded the maximum possible response. When this occurred, and the range for the lower gain setting was exceeded, data from the higher gain setting (lower sensitivity) was used. Due to the significantly higher R^2 values, the laboratory calibration was used over the field calibration (Table 3.1). All calibrations were forced through 0 to have an offset of 0. To avoid confusion, the gain settings refer to the two different OBS outputs, while the gain refers to the slope of the calibration fit. The gains derived from the calibration are shown in Table 3.1. Henceforth, all OBS derived SSC data uses the combined gain setting data, calibrated by laboratory methods.

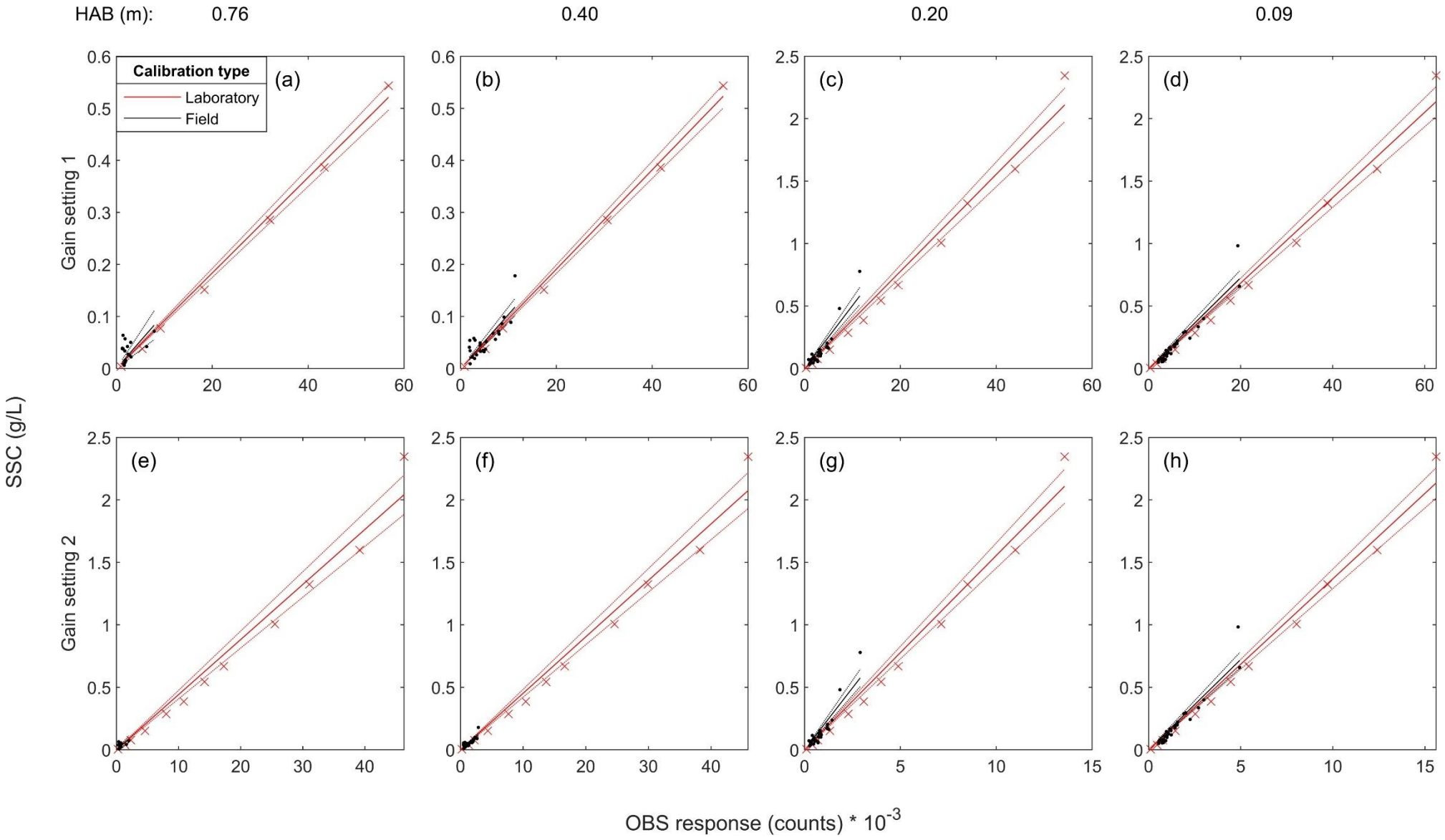

Figure 3.4: Field and Laboratory calibrations of OBS for each instrument and gain setting. Laboratory data is plotted in red with field data plotted in black. Dotted lines represent 95% confidence intervals. Derived gains and fit qualities are given in Table 3.1. All fits have an offset of 0.

Table 3.1: R^2 and gain values for each calibration fit. Instruments are denoted by their measurement height above the bed.

Instrument HAB (m)	Field				Laboratory			
	(Gain setting 1)		(Gain setting 2)		(Gain setting 1)		(Gain setting 2)	
	R^2	Gain $*10^5$	R^2	Gain $*10^5$	R^2	Gain$*10^5$	R^2	Gain $*10^5$
0.76	-0.20	1.1	-0.18	4.2	0.99	0.9	0.97	4.4
0.4	0.66	1.0	0.66	4.1	1.00	1.0	0.98	4.5
0.2	0.83	5.0	0.83	19.8	0.98	3.9	0.98	15.5
0.09	0.90	3.6	0.89	14.4	0.99	3.4	0.99	13.7

Table 3.2: Percentage difference between water sample derived SSC values, and OBS derived SSC values. SSC for the OBS is derived from a laboratory calibration.

Percent difference between water sample SSC and OBS derived SSC during the same period.

Instrument HAB (m)	0.76	0.4	0.2	0.09	
	45%	16%	75%	83%	Tide 4
	20%	2%	12%	29%	
	23%	27%	30%	33%	
	14%	16%	21%	3%	
	46%	27%	38%	45%	
	39%	3%	5%	30%	
	60%	52%	12%	36%	
	31%	110%	120%	5%	
	n/a	33%	17%	24%	
	n/a	22%	23%	44%	
	n/a	9%	38%	25%	
	n/a	n/a	6%	28%	
	n/a	n/a	13%	4%	
	n/a	n/a	n/a	1%	Tide 6
	n/a	n/a	75%	8%	
	n/a	1%	16%	7%	
	80%	5%	14%	1%	
	4%	20%	7%	18%	
	300%	34%	22%	60%	
	237%	8%	51%	30%	
	380%	119%	37%	23%	
	241%	58%	4%	10%	
	184%	133%	15%	4%	
	113%	246%	100%	10%	
	25%	81%	17%	2%	
	3%	19%	27%	13%	
	n/a	2%	13%	11%	
	n/a	10%	8%	9%	
	n/a	65%	5%	10%	
	n/a	n/a	7%	21%	
	n/a	n/a	n/a	2%	

Sampling period (end ← start)

3.3 Suspended sediment concentration

SSC was generally greater close to the bed and decreased with height above the bed (Figure 3.5). Additionally, SSC was greater at the start and end of each tide reaching maximum values of around 0.9 g/L when water depths were low. Typically, concentrations were smallest around high tide (slack water). This pattern is generally true for all measurement heights; however, the difference across the tide was significantly more pronounced closer to the bed. Generally (tides 2-6), the maximum SSC occurred on the incoming tide while the outgoing tide had a smaller SSC peak. However, the converse was observed during the first tide.

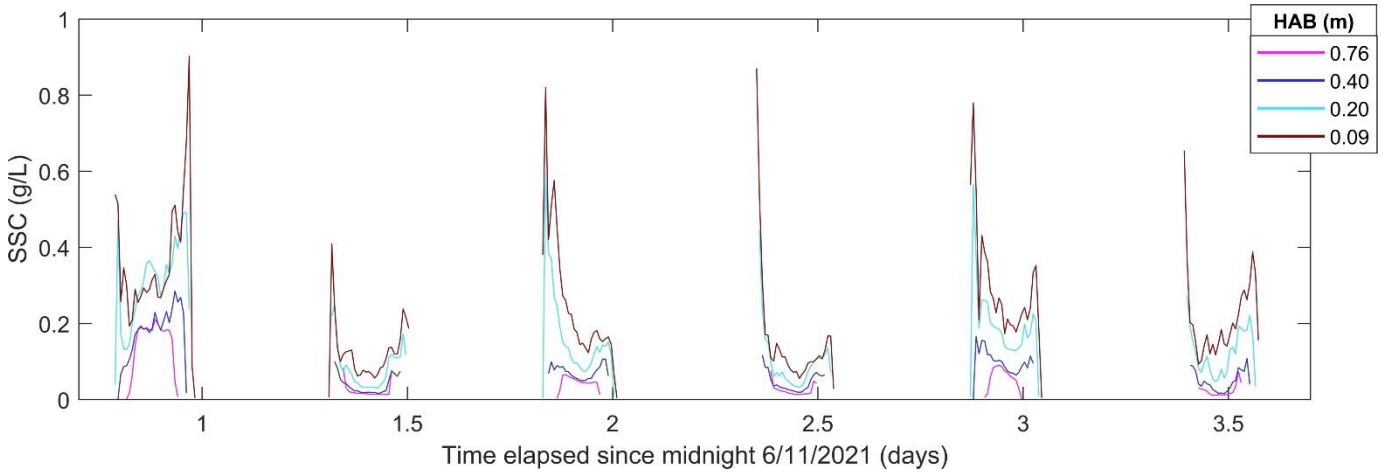

Figure 3.5: Time series of SSC for each of the 4 instruments.

Figure 3.6 presents SSC and velocity data in the context height in the water column. Here the initial pulses of sediment can be seen at a low elevation during the initial and final stages of each tide. Across shore velocity (Figure 3.6 (b)) can be seen favouring onshore flow (associated with the flood tide) at higher elevations and offshore flow (associated with the ebb tide) at lower elevations.

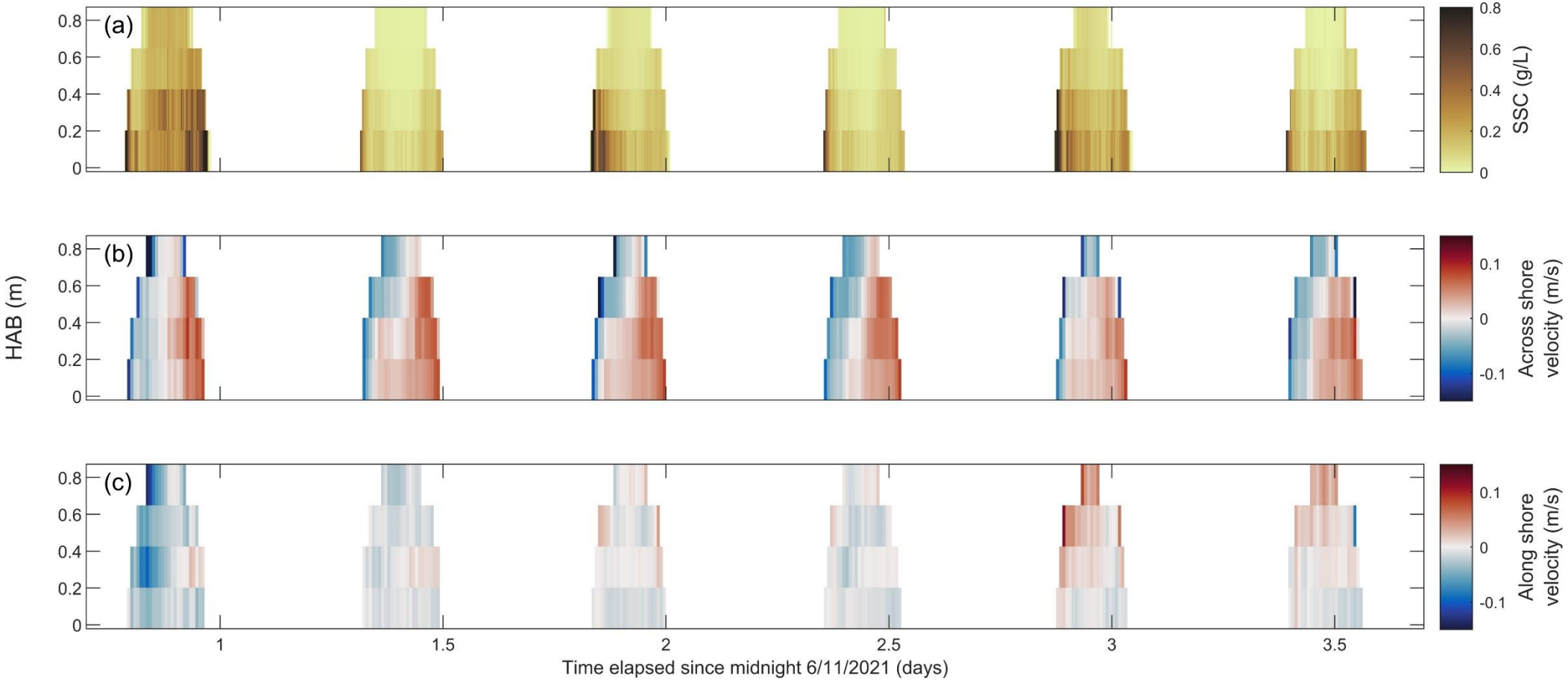

Figure 3.6: Time series colour plot of SSC (a) and velocities (b, c). Velocities are rotated to run across and along the shoreline as opposed to N-S and W-E. The shoreline is oriented roughly West to East (Figure 2.1). Positive across shore velocity values represent offshore currents while negative values represent onshore currents. Positive along shore velocity values represent flow roughly toward the east while negative values represent flow toward the west.

SSC profiles derived from the inversion of ABS data were provided by Redder (2023). For good bursts (i.e., Figure 3.7), ABS derived profiles fit the upper two OBS values well (0.4 and 0.74 meters above the bed), while estimating a significantly greater SSC than the lower OBS (at 0.2 metres above the bed). It should be noted that due to the methods used by Redder (2023) to obtain SSC from the ABS, the results are tuned to the upper two instruments. In terms of the OBS at 0.09 m, the ABS derived SSC profile did not extend to said height due to the height of the bed mounted transducers. ABS data is used to compare SSC derived from the ABS and OBS instruments.

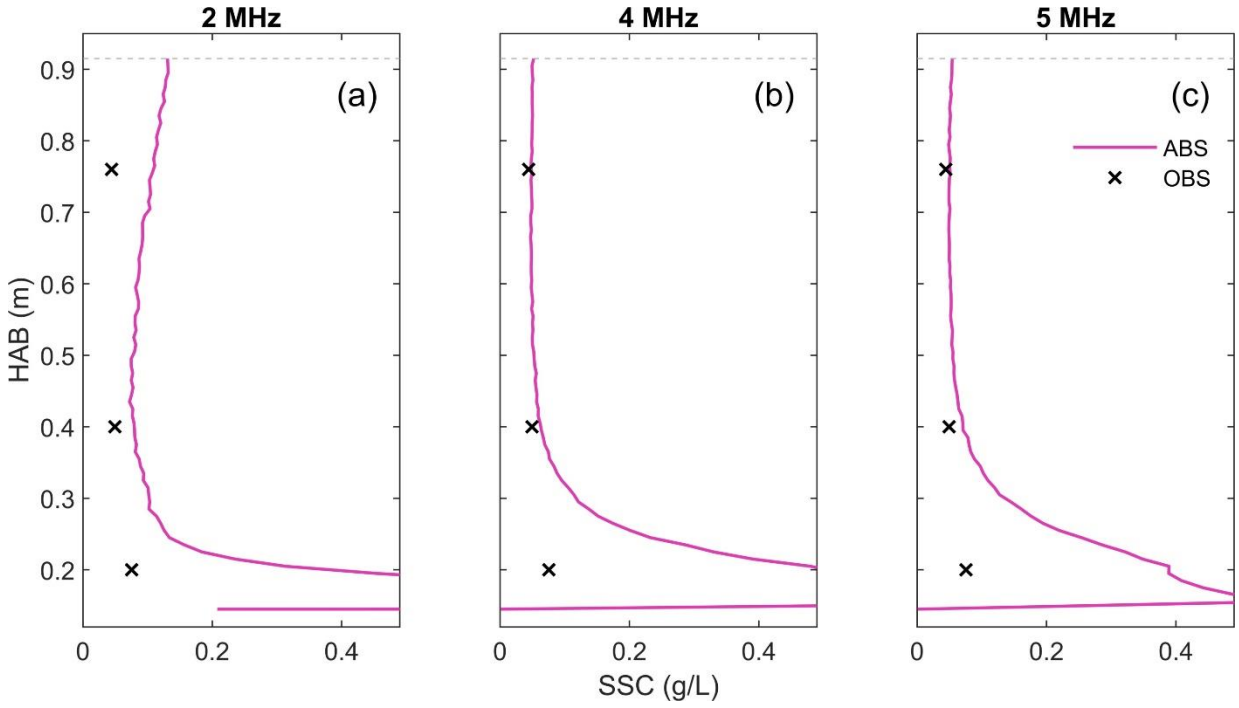

Figure 3.7: SSC derived from ABS and OBS for ABS transducer frequencies; 2 Hz (a), 4 Hz (b), and 5 Hz (c). Dotted lines represent water level. Data was taken from a burst during tide 3 at approximately 22:10.

3.4 Comparison of measured velocities

Velocity was measured by three types of instrumentation, an Aquadopp, Signature, and Vectors, all within a ˜20 m radius (Figure 2.1). Velocity trends across instruments, such as onshore flow during the flood tide and offshore during the ebb, were generally in agreement. Along-shore velocities showed more variability across instruments and fewer discernible patterns than across-shore velocities.

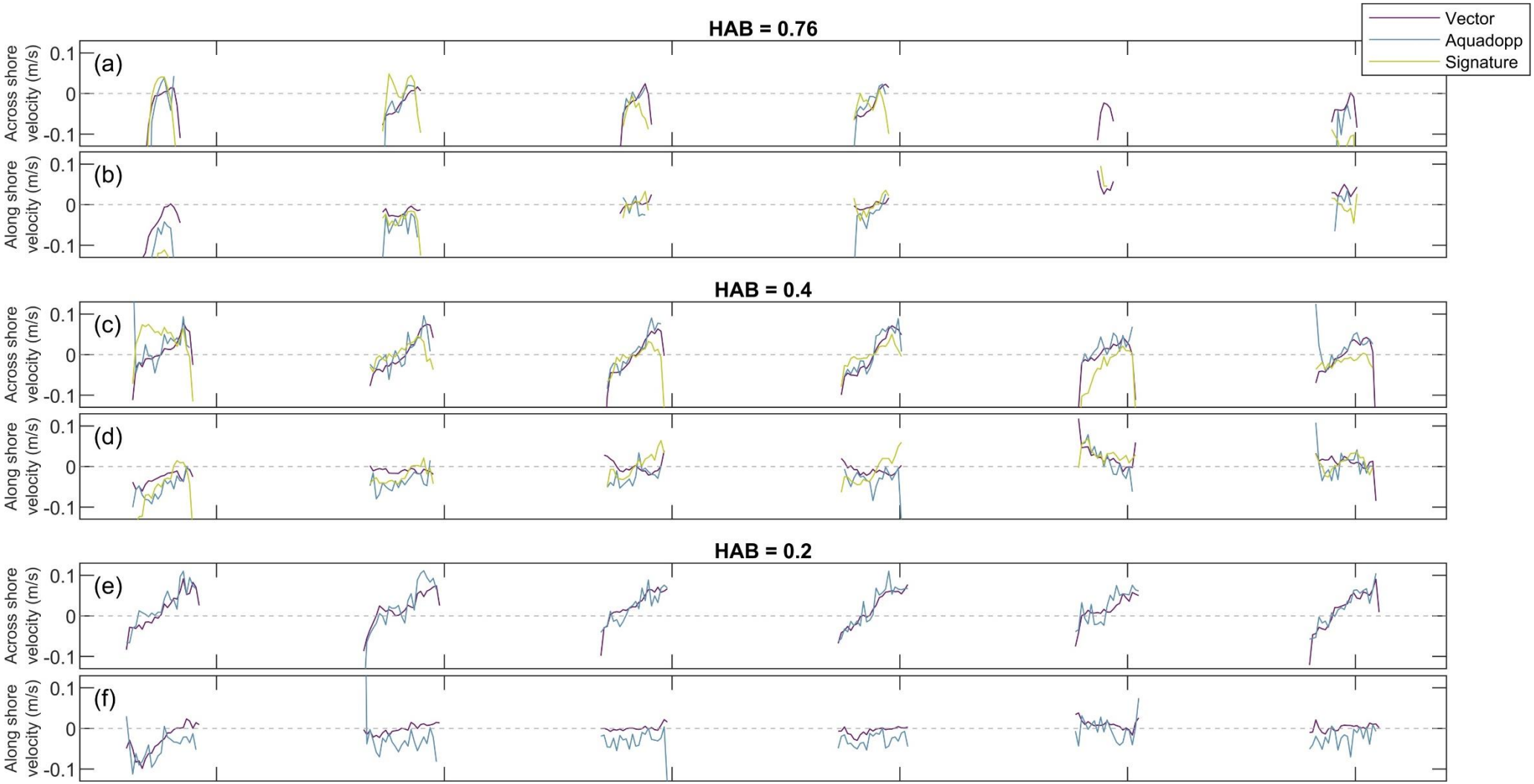

Figure 3.8: Across and along shore velocities for each instrument at 0.76, 0.4 and 0.2 m above the bed. Negative across shore values represent onshore flow while positive values represent offshore flow. Negative along shore velocity values represent flow roughly toward the west while positive values represent flow toward the east.

3.5 Velocity model

The law of the wall was primarily fit to Vector derived velocity profiles (Figure 3.9). The goodness of fit is represented by the sum of the square errors (SSE). SSE for the law of the wall varied significantly indicating variation in how well the model represented our data. In general, the fit was worse (had larger SSE values) when *Hs* was elevated (i.e., during tides 3 and 5, and especially during tide 1) (Figure 3.10). A full set of velocity profiles measured by the Vectors with the associated law of the wall profile for each burst can be found in the appendix.

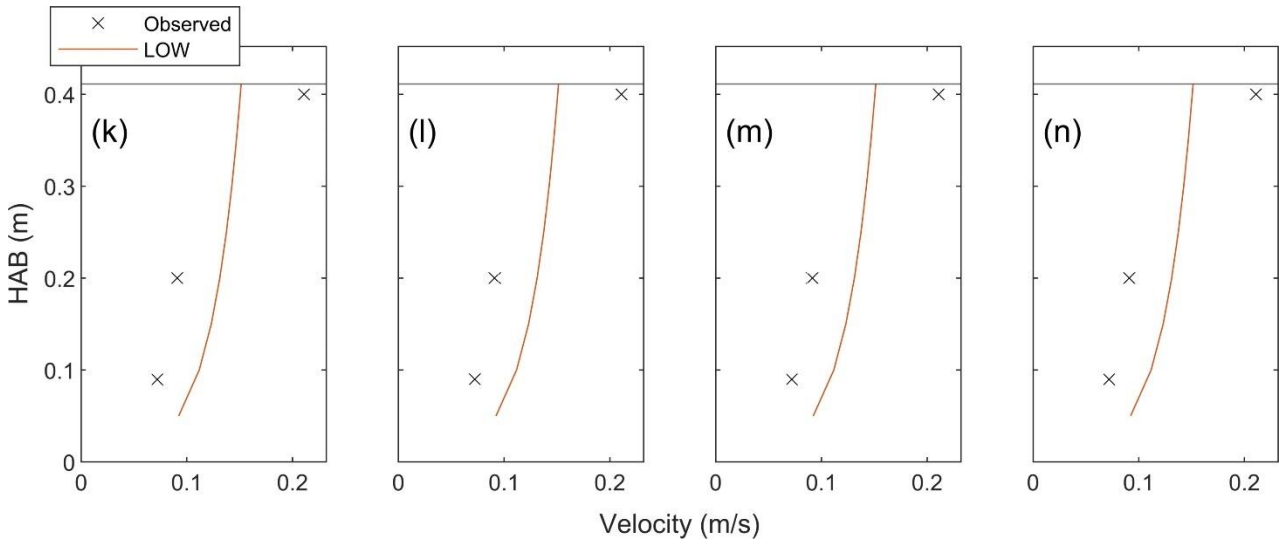

Figure 3.9: Profiles of observed velocity data and the law of the wall (LOW) calculated from said data. The horizonal line represent the water height. Profiles were taken from 4 bursts during tide 6.

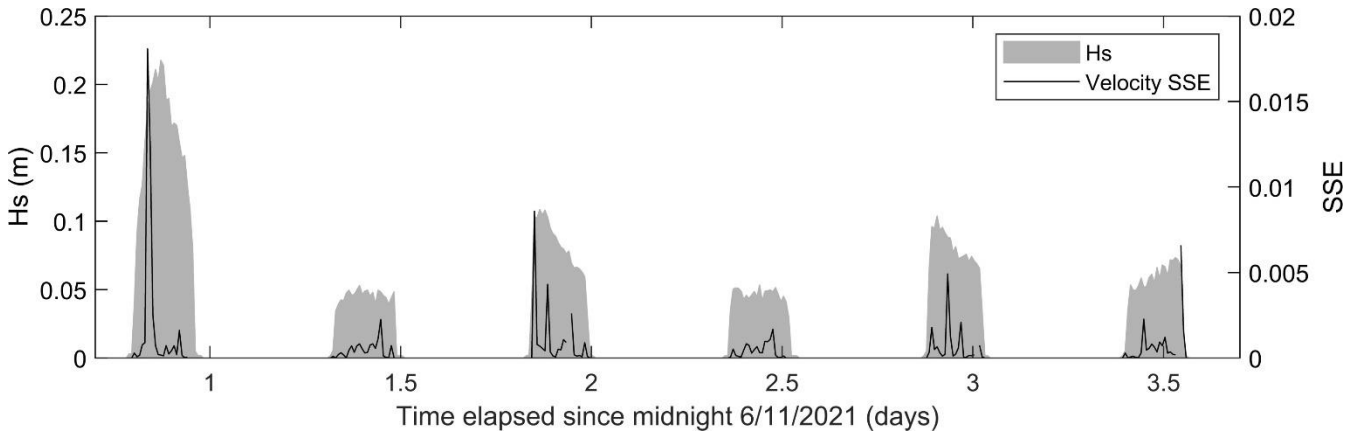

Figure 3.10: Significant wave height (Hs) in grey plotted behind the law of the wall SSE in black.

In addition to Vector data, Signature and Aquadopp data was fit to the law of the wall in order to calculate $\bar{u}^*$, z_0, and C_D for each instrument individually. The majority of Aquadopp derived velocities fit poorly ($R^2 < 0.8$), and as such were discarded. Furthermore, to ensure accurate values of $\bar{u}^*$, z_0 and C_D any Vector or Signature fits with $R^2 < 0.8$ were also discarded.

$\bar{u}^*$ predominantly ranged from 0 to 0.2 m/s with data derived from the Signature generally being greater than that derived from the Vectors (Figure 3.11). z_0 values, for the majority of data, ranged from 0 to 0.4 m, with Signature values being greater (Figure 3.11). However, for a small portion of data, values of z_0 derived from the Vectors were very large, reaching 2.4 m. For C_D (dimensionless) most values ranged between 0 and 0.2 with a few values from the Vectors reaching as high as 1.8.

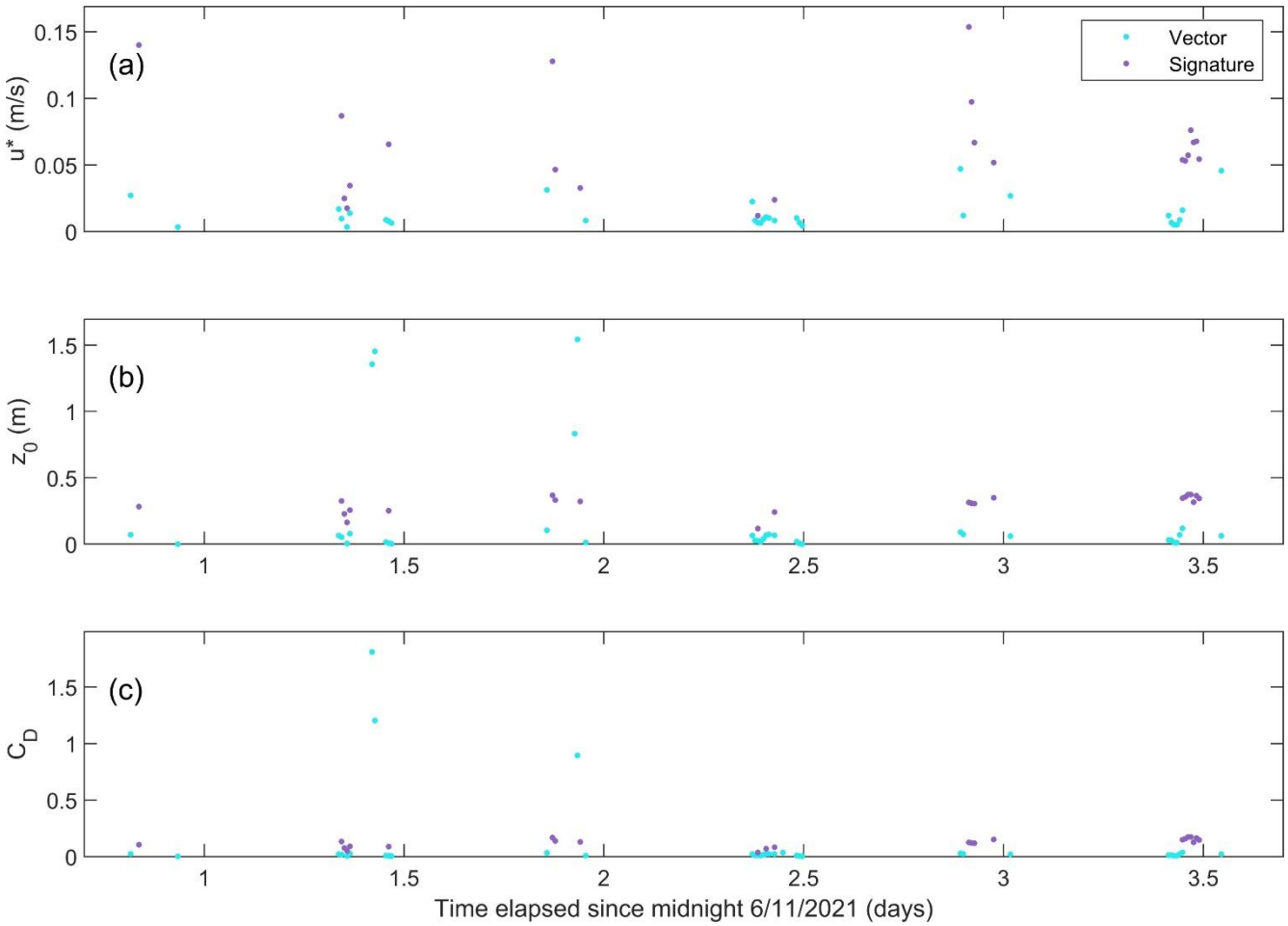

Figure 3.11: Time series of friction velocity $\bar{u}^*$ (a), hydraulic roughness z_0 (b), and the drag coefficient C_D (c), from two different instruments. All values are derived from bursts during which velocity fit well ($R^2 > 0.8$) to the law of the wall.

Figure 3.12 displays data from an example burst, where velocity data from the Signature and Vectors fit ln(z) and the law of the wall well ($R^2 > 0.95$). $\bar{u}^*$, z_0, and the C_D during this burst did display significant differences per instrument. In addition, the Vector data fit the law of the wall slightly better than that of the Signature.

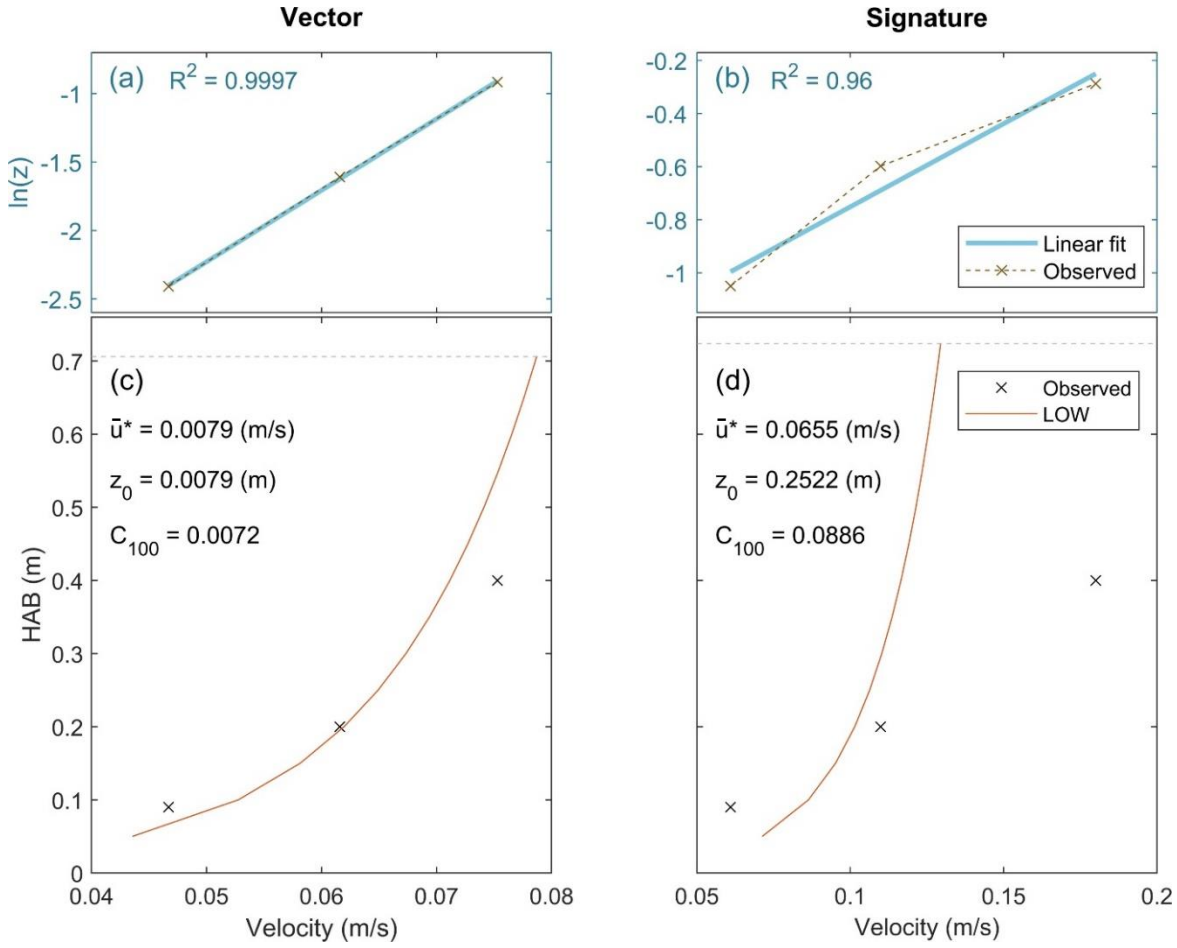

Figure 3.12: velocity data from burst 109, fit to the law of the wall (c, d) and ln(z) (a, b). friction velocity $\bar{u}^*$ and hydraulic roughness z_0 are derived from the slope and intercept of the linear fit of velocity to ln(z). The drag coefficient, C_D, is derived using z_0. The dotted line in panels c and d denotes water depth.

3.6 SSC Model fits

Three different SSC models were fitted to the observed SSC, assuming constant diffusivity, linear diffusivity, and parabolic diffusivity, respectively (Figure 3.13). Figure 3.13 displays example profiles taken from 4 bursts during tide 6. Tide 6 is chosen because it is fairly representative of the other tides. In general, the SSC models fit the data very well, and this was true for most bursts. A full set of SSC profiles measured by the OBS with the associated model profiles for each burst can be found in the appendix.

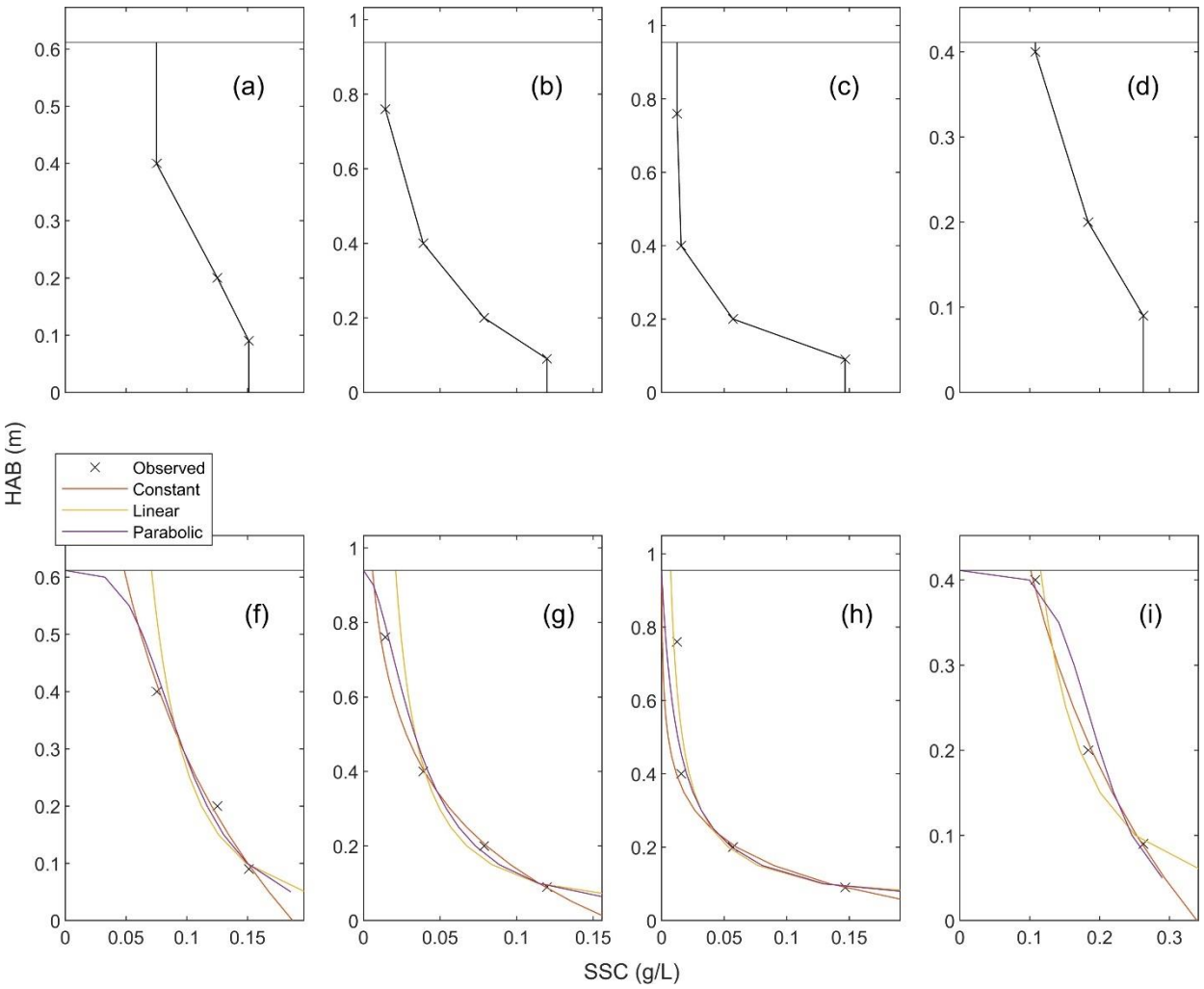

Figure 3.13: SSC profiles (a – e) and model profiles with SSC plotted on top (f – j). SSC models assume constant, linear, and parabolic diffusivity. The horizontal line represents the water surface at the time of the burst. Each column of plots represents a burst during tide 6.

The SSE was also used to describe the goodness of fit for each of the SSC models to the observed data. In general, SSE did not display a strong relationship with wave height; however, average SSE was consistently larger during tides with larger average wave heights (Figure 3.10).

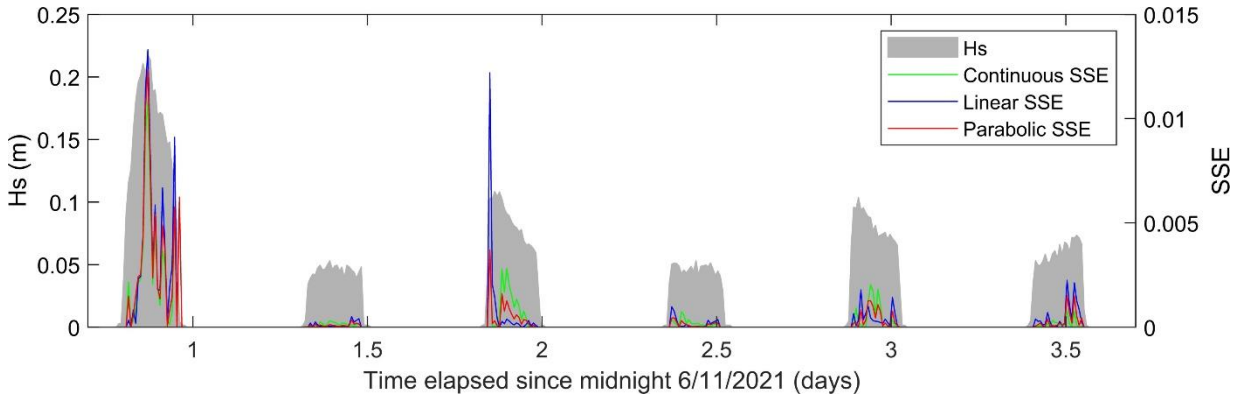

Figure 3.14: SSE for continuous, linear, and parabolic diffusivity models, plotted over significant wave height (Hs) in grey.

3.7 Time series of sediment fluxes

Figure 3.15 shows the fluxes resulting from Ex1, Ex2, and Ex3 during tide 6. Tide 6 was chosen for display purposes as it was representative of the majority of other tides. For tide 6, Ex3 makes up a very small proportion of Ex1, while Ex2 accounts for the majority of the extrapolated flux. However, for total fluxes over the full deployment period, Ex2 and Ex3 increased flux onshore and offshore, respectively, by similar amounts.

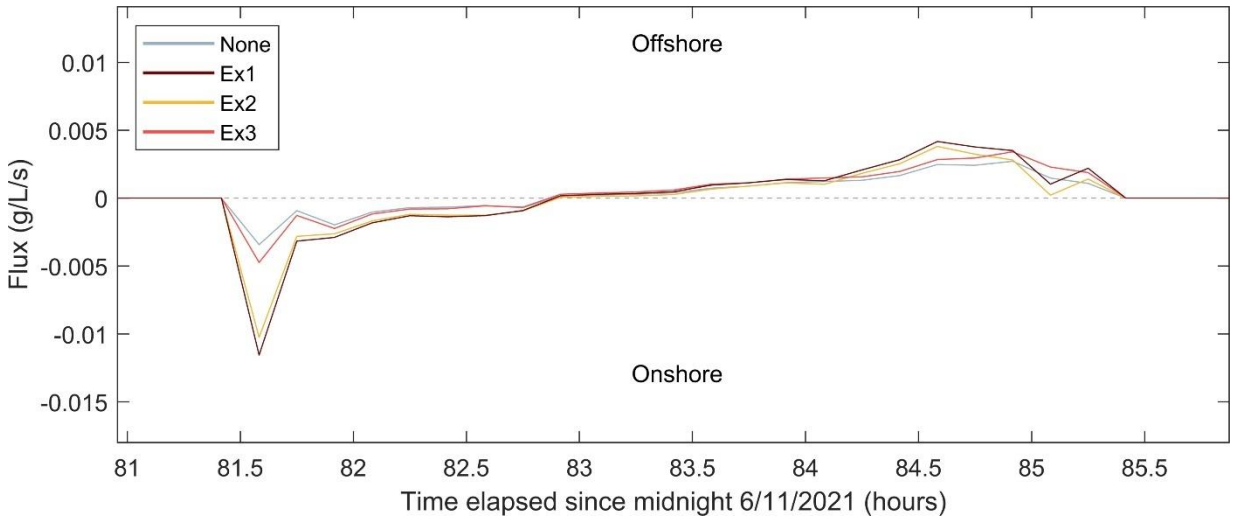

Figure 3.15: Time series of flux for Ex1, Ex2 and Ex3 during tide 6. Negative values represent onshore flux while positive values represent offshore flux.

Ex4, Ex5, Ex6, and Ex7 extrapolate using different combinations of instruments at different heights above the bed (Figure 2.6). In all cases, for total flux and tide 6 flux, the result was an increase in offshore flux. Total flux increased in the offshore direction by

between 6.5 and 2 times (Table 3.3). As seen in Figure 3.16 with the extrapolations of interest, flux becomes predominantly offshore during the majority of the tide, which is also true for other tides. The increase in offshore flux got smaller from Ex4 to Ex7.

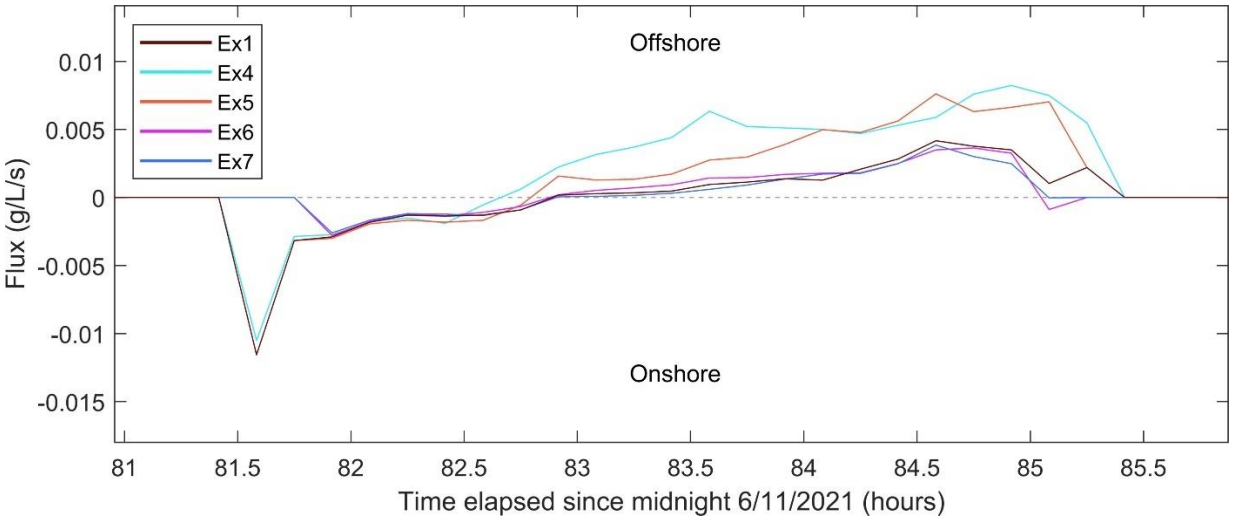

Figure 3.16: Time series of flux for Ex1, Ex4, Ex5, Ex6 and Ex7 during tide 6. Negative values represent onshore flux while positive values represent offshore flux.

Figure 3.17 compares Ex8, Ex9, and Ex10 with the reference case Ex1. Ex8, Ex9, and Ex10 extrapolate SSC in the same manner as Ex4, Ex5, and Ex6, respectively, while using the full velocity profile (equivalent to Ex1) (Figure 2.6). For Ex8 to Ex10 onshore flux increased, an effect that was consistent across tides. The increase in onshore flux got smaller from Ex8 to Ex10. In general, the change in flux from Ex1 was smaller for Ex8 to Ex10 than Ex4 to Ex6 with the equivalent SSC profile (Table 3.3).

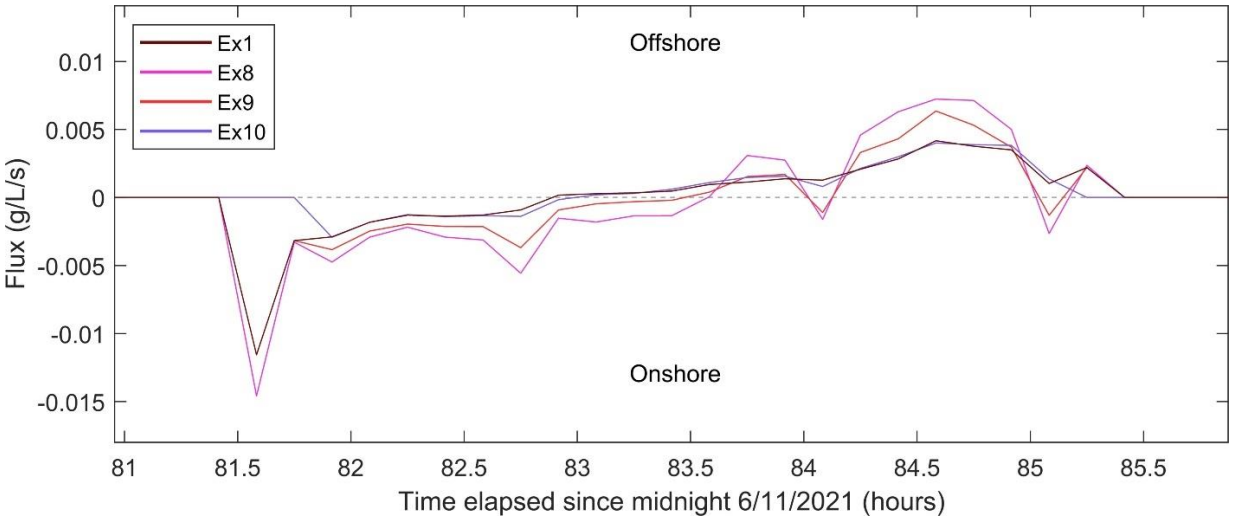

Figure 3.17: Time series of flux for Ex1, Ex8, Ex9, and Ex10 during tide 6. Negative values represent onshore flux while positive values represent offshore flux.

Table 3.3 Flux totals for each extrapolation method in addition to the percent change compared to the primary reference extrapolation; Ex1. Totals and % change given for full time series as well as only tide 6. Negative values indicate onshore flux while positive indicate offshore.

Extrapolation type	Full time series		Tide 6 time series	
	Total flux	% Difference	Total flux	% Difference
None	0.054	12%	0.008	700%
Ex1	0.048	0%	0.001	0%
Ex2	0.025	- 48%	-0.002	- 300%
Ex3	0.076	58%	0.011	1000%
Ex4	0.364	658%	0.059	5800%
Ex5	0.283	490%	0.035	3400%
Ex6	0.110	129%	0.014	1300%
Ex7	0.095	98%	0.01	900%
Ex8	-0.075	- 256%	-0.011	- 1200%
Ex9	-0.017	- 135%	-0.006	- 700%
Ex10	0.054	12%	0.014	1300%

A time series of sediment flux is presented in Figure 3.18 with onshore and offshore flux represented by negative and positive values, respectively. Over all 6 tides, fluxes peak onshore at the start of the tide and offshore at the end. In most cases, the onshore peak reaches larger maximum values than the offshore peak of the same tide. Flux generally changes from going onshore to going offshore halfway through the tide (slack tide), however, in some cases this switch does not occur at slack tide, or alternates between onshore and offshore flux for a significant period of time. For example, during the start of tide 5, where flux switches from onshore to offshore and back during the flood portion of the tide.

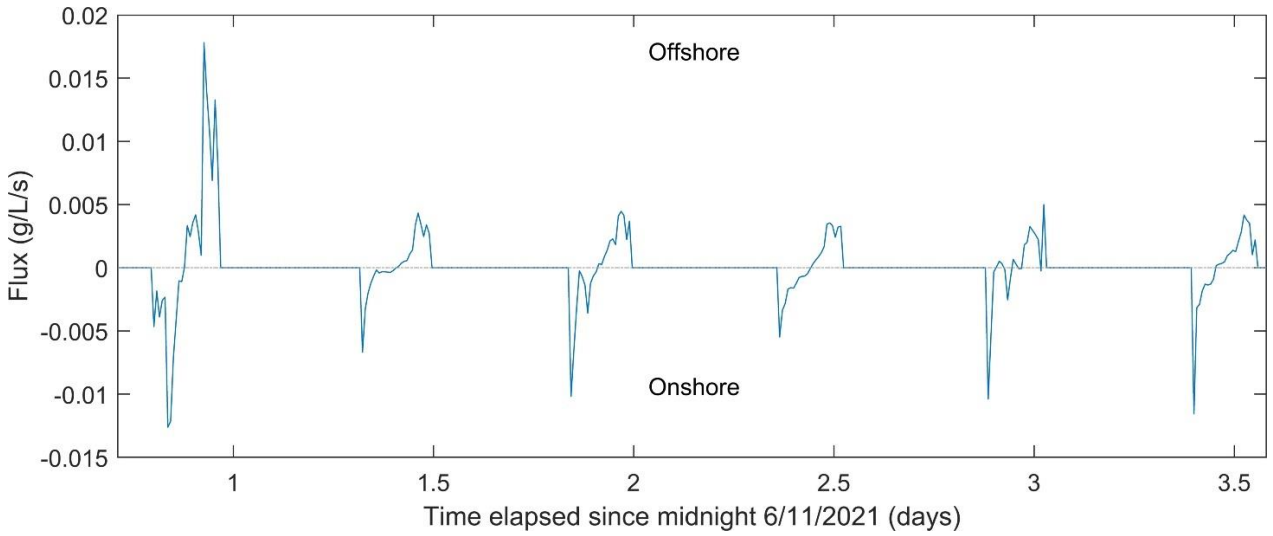

Figure 3.18: Time series of flux. Negative values represent onshore flux while values positive represent offshore flux.

Figure 3.19 plots the breaker ratio which is calculated as $\frac{Hs}{h}$, where *Hs* is significant wave height and *h* is water depth. Peaks in the breaker ratio line up roughly with peaks in sediment flux. Peaks in the breaker ratio occur at the start of the flood tide and end of the ebb tide when water depths are lowest. These peaks are not as well-defined during tide 1 as the other tides, due to the larger waves that increased in size over slack tide, effectively dampening out the start and end of tide peaks.

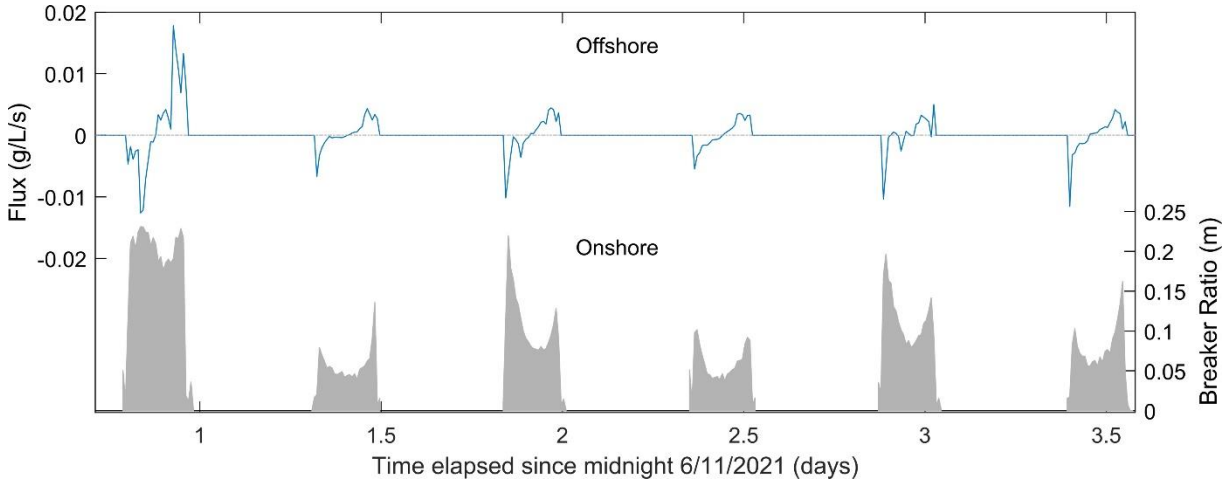

Figure 3.19: Time series of flux plotted above the breaker ratio (Hs/h). Negative values represent onshore flux while positive values represent offshore flux.

Total flux per tide was usually offshore, except for tide 3, during which flux was onshore but very small in comparison (0.0004 g/L/s). Flux during tide 1 coincided with significantly larger wave heights than the other tides (Figure 3.20). Total flux during tide 1 was significantly larger than all other tides (approximately 15 times larger).

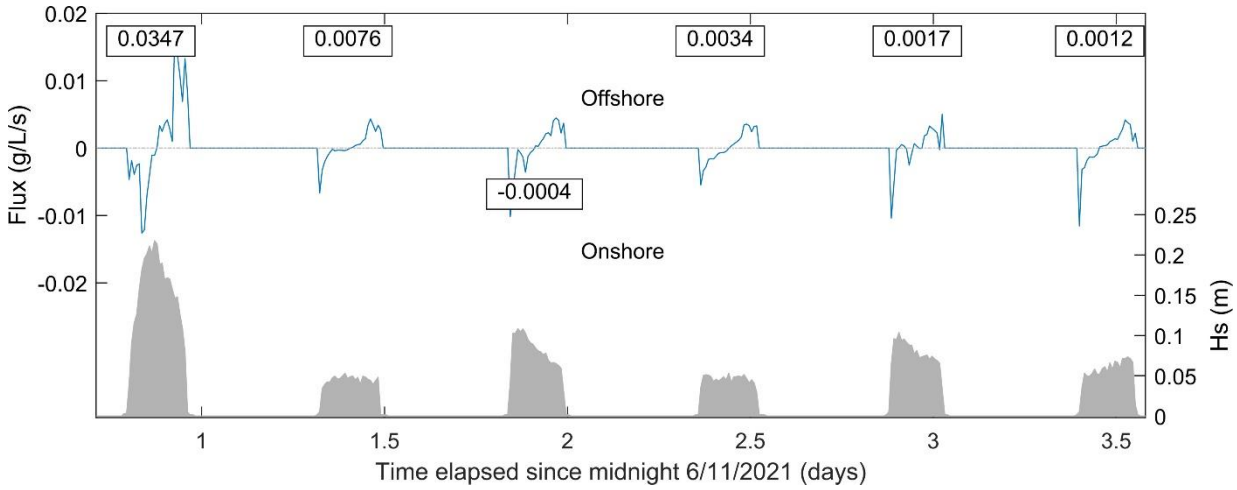

Figure 3.20: Time series of flux plotted above significant wave height (Hs). Total flux values for each tide are displayed along the flux time series in g/L/s. Negative values represent onshore flux while positive values represent offshore flux.

In addition to the "normal" flux estimates, derived from the Vector and OBS measurements, flux was estimated from the model SSC and measured Vector velocity data. The fluxes resulting from each model were very similar (total fluxes within 0.01 g/L/s of each other) and because of this, for display purposes, only flux estimated using the continuous diffusivity model is presented (Figure 3.21). Total flux over the time series was 0.06 g/L/s, an increase in offshore flux compared to the reference flux. Despite this, absolute values for the flux derived from continuous diffusivity were lower than the absolute values of the reference flux (i.e., the reference flux reached larger onshore and offshore maximum values each tide).

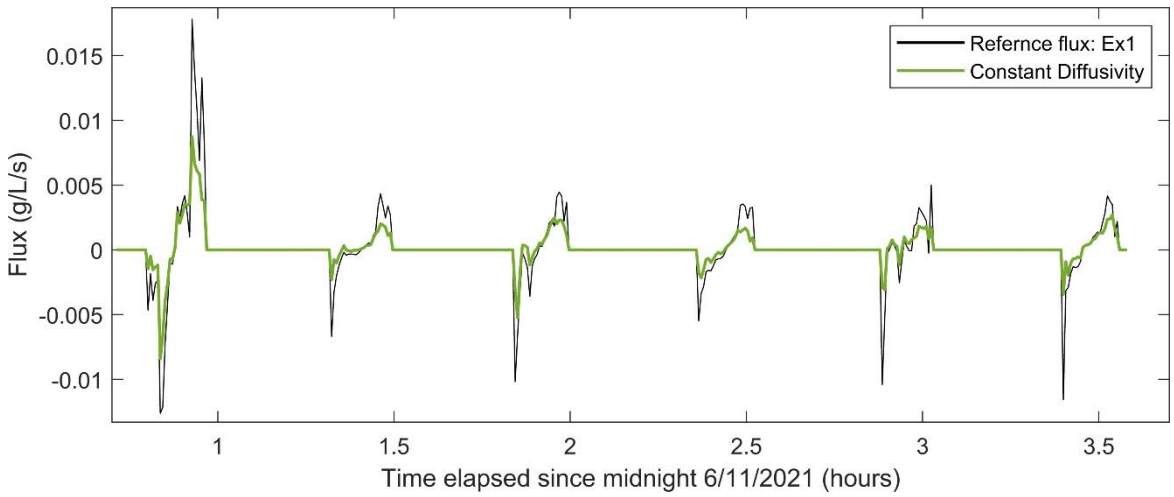

Figure 3.21: Time series of flux estimated using SSC values derived from the constant diffusivity model, and velocities derived from the Vector measurements. Negative values represent onshore flux while positive values represent offshore flux.

Chapter 4: Discussion

4.1 OBS Calibrations

Each method of OBS calibration (field and laboratory) has advantages and drawbacks. The laboratory calibration is commonly used throughout literature (Kleinhans et al., 2009; Nowacki & Ogston, 2013) allowing for the manual selection of calibration ranges, thus ensuring that the vast majority of data falls within the calibration bounds. Our calibration covered SSC values between 0.004 and 2.35 g/L with 99.9% of recorded SSC data falling below 2 g/L. In comparison, calibrating from water samples collected in the field during the experiment has the benefit of better representing the properties of the suspension (e.g., in-situ particle size distribution) being observed by the OBS. However, it is not always possible to control spatial variability in SSC as it is in the laboratory. While some researchers have had success with field calibrations (Andersen & Pejrup, 2001; MacVean & Lacy, 2014), in general, the added variability increases the chance of a poor calibration compared to laboratory methods. Additionally, a field calibration is unlikely to cover the highest SSC peaks due to limited temporal coverage. From the highest to lowest instrument, our field calibration covered 75.8, 88.3, 99.6, and 99.5 % of SSC data, respectively. While the lower two instruments had good resulting field calibrations, with R^2 values comparable to the laboratory calibrations (Figure 3.4), the field calibrations for the upper two instruments were poor, especially that of the highest instrument (Table 3.1). Due to spatial variability of SSC, it is possible that some variability was introduced by sampling from an intake tube which was offset horizontally (but still within ˜0.5 m) from the OBS measurement location. Additionally, the upper two sensors would have been affected by wave flow to a greater degree, likely increasing the high frequency temporal variability of the signal at these heights. In general, field calibrations calculated greater SSC values than laboratory calibrations with an average increase of 15 %.

4.2 Instrument variability

Two main comparisons between instruments were made. Firstly, comparing SSC measurements between OBS and ABS, and secondly, comparing velocity profiles between the Signature, Aquadopp, and the array of Vectors. Measurements across instruments generally agreed in trend and magnitude, however, the agreement of these measurements varied significantly both spatially and temporally.

4.3 SSC and velocity

SSC values were comparable to those recorded by other researchers (Dyer et al., 2000; MacVean & Lacy, 2014) under similar conditions and at similar locations on the cross-shore profile of the intertidal flat. During the deployment period, maximum burst-averaged SSC values reached 0.9 g/L with 91% of values falling below 0.3 g/L. These values were very similar to those recorded by Lovett (2017), whose observed values were typically around 0.2 g/L during calm periods with few waves. In contrast, during wavy periods Lovett (2017) commonly observed values in excess of 1.5 g/L. Despite the much greater SSC values, waves during Lovett's (2017) deployment only reached 0.3 m, comparable to the largest waves observed during our study.

In general, SSC was larger closer to the bed (Figure 3.5) in accordance with the Rouse profile (Rouse, 1937) and in alignment with findings from other researchers (Bassoullet et al., 2000; Ralston & Stacey, 2007). The first tide had the overall greatest SSC values (Figure 3.5), likely as a result of greater wave activity during that period (Figure 3.3). Greater wave activity results in stronger wave orbital velocities at the bed (Figure 3.3 (a) and (c)) which increases bed shear stress, thus suspending more sediment and therefore increasing SSC. Various other researchers have also linked greater wave activity to larger SSCs (Bassoullet et al., 2000; Nowacki & Ogston, 2013). Across all tides, a pulse of elevated SSC occurred at the start of the flood, and end of the ebb tide (Figure 3.5). The SSC pulses resembled those described by Christie & Dyer (1998), who describes a so-called "turbid fringe" on the leading edge of the incoming tide. Within the turbid fringe, water depth is very shallow, and as such, even very small waves have the ability to penetrate the bed and resuspend sediment (Green & Coco, 2014). As a result, the SSC in the turbid fringe is very high, which is what we observe on the leading edge of the tides in our study. As stated in Christie & Dyer (1998), the initial SSC pulse on the flood tide results from the resuspension of a low-density biofilm and sediment off the bed, in combination with, elevated current velocities associated with the initial stages of the tide, and greater wave induced shear stresses resulting from the low water depth. The second SSC pulse at the end of the ebb tide that we observe, likely results from similarly heightened velocities and wave activity, in combination with, the mixing of high concentration suspensions near the bed that form due to settling over the slack water period. In tides 2-6, larger SSCs were observed during the flood tide than during the subsequent ebb tide, which is commonly concurrent with other research observing the

same tidal variation in SSC (Black, 1999; Dyer et al., 2000; Uncles & Stephens, 2010). The discrepancy in the pattern during the first tide is possibly due to greater wave induced mixing, as wave orbital velocities were greater overall during the first tide. However, these orbital velocities did not display the minor increases coinciding with SSC pulses during tide 1 as they did for the other tides (Figure 3.3 (a)).

4.4 Model fits

For the majority of bursts, Vector and Signature data fit the law of the wall poorly (74 % of data had an $R^2 < 0.8$). In similar environments, various other researchers have also found the law of the wall to be non-representative of the majority of their data, i.e., MacVean & Lacy (2014) and Collins et al. (1998). The poor correlation to the law of the wall elucidates the possibility for error when extrapolating velocity from a single height over the water column using a logarithmic framework (i.e., Bassoullet et al. (2000)).

In general, $\bar{u}^*$, z_0, and C_D overlapped between the Vector and Signature, however, the Signature typically estimated greater values for all variables. The Signature usually estimated C_D to be between 0.04 to 0.2. The Vectors on the other hand, ignoring a few very large values, typically estimated C_D to be between 0 and 0.04. For reference, 0.0025 is the typical C_D applied to flat, cohesionless seabeds (Green et al., 1998). Several C_D estimates fell close to 0.0025, with the closest estimate being 0.0023. z_0 values were around 20 cm, which corresponds well to the height of the large bedforms observed in the field.

In general, the SSC diffusivity models fit the data fairly well, while the fit between the velocity data and the law of the wall contained more variability (Figure 3.13). The SSC model fits were generally worse during the first tide when wave energies were greater. This decrease in fit quality is due to the Rouse profile models not accounting for wave re-suspension, and as such, care must be taken when applying said models during periods of increased wave activity. The SSC derived from the diffusivity models was fairly similar to the measurement derived SSC, with an average difference of approximately 20%. This demonstrates that under calm conditions, SSC diffusivity models can provide a good approximation for fluxes.

4.5 Flux sensitivity

Sediment flux per tide was predominantly offshore with the exception of tide 3, over which, net flux was onshore but very low at 0.0004 g/L/s. Additionally, the majority of flux over the duration of the experiment occurred during tide 1, which accounted for approximately 73% of total flux at 0.347 g/L/s (Figure 3.20). This result suggests that wave activity is responsible for driving erosion on the flat. Many studies have found wave activity to induce erosion on intertidal flats; however, they also usually observe onshore flux and deposition during calm periods (Andersen & Pejrup, 2001; Ralston & Stacey, 2007). This result is contrary to our observations, in which, even under calm conditions with wave heights on the order of 10 – 15 cm, flux was usually offshore indicating erosion. Other studies of the Firth of Thames mud flat have also observed offshore flux just beyond the forest edge, in addition to onshore flux within the forest (Lovett, 2017). In combination with long term bed elevation data showing the flat to be accretional over decadal time periods, it appears that the flat accretes by scouring in front of the mangroves and depositing within the forest (Figure 4.1).

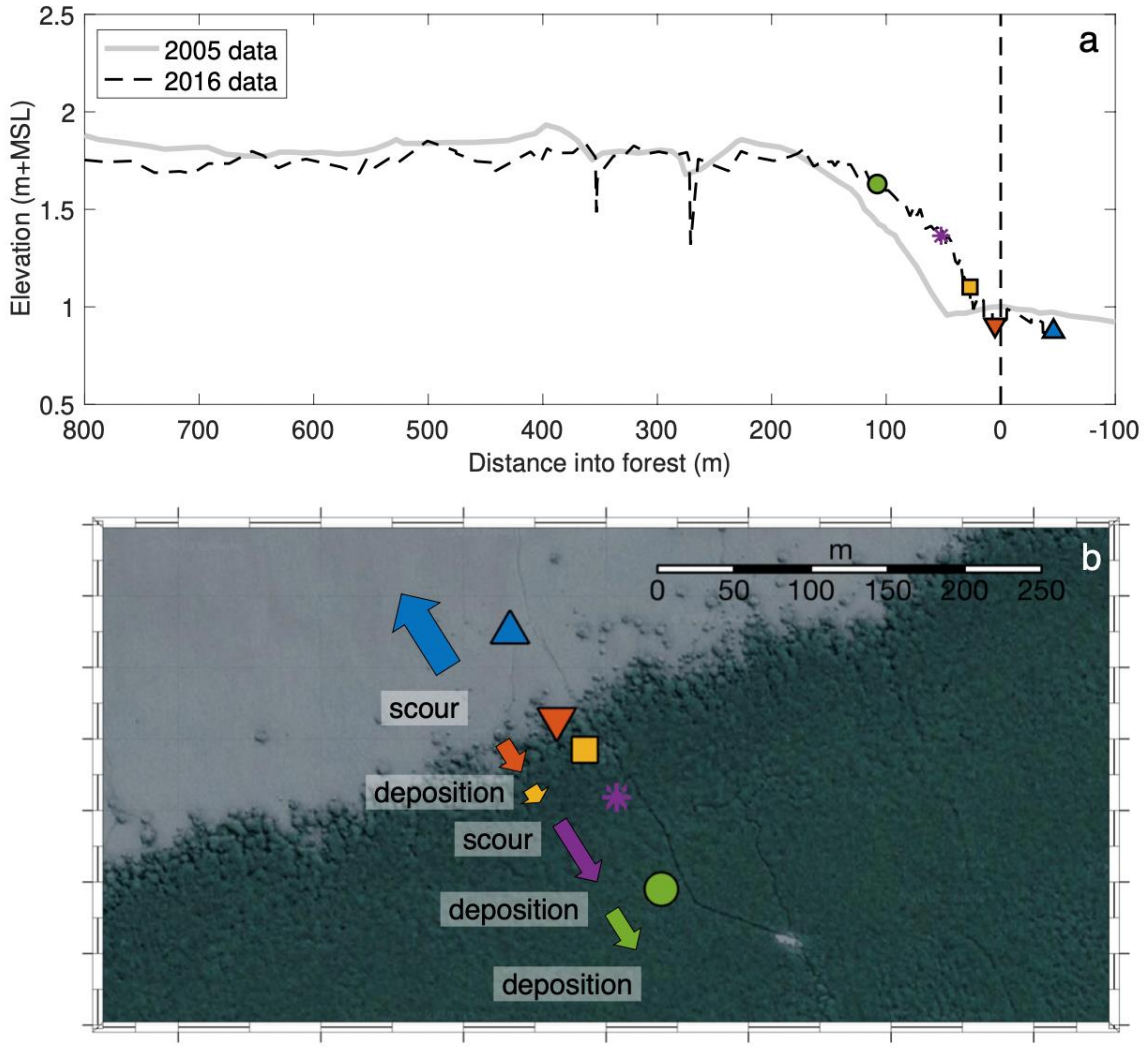

Figure 4.1: Elevation profiles from 2005 and 2016 (a). Satellite imagery of site with arrows representing sediment fluxes. Arrow direction represents flux direction while arrow size represents the magnitude of cumulative fluxes (approximately). Taken from Mullarney, (pers comm.).

In general, on the scale of total flux per tide, fluxes were sensitive to changes in the extrapolation technique (Table 3.3). It should be noted that the closer to 0 net flux of the primary extrapolation (Ex1) is, the more exaggerated the percentage difference will be. For example, the percentage differences for tide 6 were very large due to the reference extrapolation (Ex1) being small (0.001), and as such, even a small increase in flux results in a large percentage difference. The primary extrapolation displayed a relatively small difference to the no extrapolation case. This result is due to the upper and lower portions of the extrapolation increasing flux in opposing directions, and thus cancelling each other out. The upper portion of the extrapolation increased onshore flux, while the lower portion increased offshore flux by a similar amount.

Extrapolations Ex4-Ex7 demonstrate how flux estimates would differ under a different number of instruments, at different heights above the bed. Ex4 extrapolates using data from only the lowest instrument at 0.09 m above the bed. Ex4 would be analogous to single instrument setups close to the bed, such as that used by Andersen & Pejrup (2001) or Nowacki & Ogston (2013). Based on the significant increase in flux under Ex4 compared with Ex1, such an arrangement of instruments is highly likely to overestimate net flux. The degree of error will be less in a well-mixed system, such as that studied by Nowacki & Ogston (2013). However, the degree of mixing, and thus error, is still uncertain.

The observed increase is mostly resultant from the greater SSCs closer to the bed that are then extrapolated throughout the water column. The difference between Ex1 and Ex4 was the greatest of all the extrapolations, and this was consistent across all tides except for tide 1. Extrapolations Ex5-Ex7 are analogous to instrument arrangements monitoring two heights (i.e., Colisimo et al. (2020) and Yamada et al. (2009)), and in general were closer to Ex1 than Ex4. From extrapolations Ex5 to Ex7, the height of data used for the extrapolations increased and the difference to Ex1 decreased, respectively. As such, it appears that a more even spread of instruments throughout the water column gives better estimates of flux; however, this relationship is likely highly dependent on the hydrological characteristics of the intertidal zone in question.

Extrapolations Ex8-Ex10 demonstrate flux estimates from a full set of 4 velocity instruments in combination with 1-2 SSC measurements (i.e., MacVean & Lacy (2014)). In general, estimates were closer to Ex1 than extrapolations with the same SSC data points but less velocity data (extrapolations Ex4-Ex7). Ex8 and Ex9 both produced onshore flux estimates as opposed to offshore.

Chapter 5: Conclusions and future recommendations

5.1 Conclusions

Several conclusions were drawn from this work and are presented in the following;

1. While the in-situ OBS calibration was intended for primary use, it was rejected due to the poor fit of the calibration to the data. As such, it was necessary to revert to using the more reliable lab calibration.
2. Greater wave activity increases fluxes significantly, while also decreasing the quality (goodness of fit) of the SSC and velocity models explored in this study.
3. In general, the SSC models discussed in this study fit the data well and as such, would theoretically be reasonable to use for flux calculations (given calm conditions).
4. Sediment fluxes for our study were highly sensitive to the extrapolation method used (analogous for the instrument number and arrangement), and as such, it is suggested that sediment fluxes for other studies will also be sensitive to the extrapolation method.
5. Based on the least sensitive extrapolation methods, the accuracy of flux data tends to increase with the number of SSC and velocity data points in the profiles used to calculate flux. In addition, a more even spread of instruments over the water column appears to give a more accurate estimate of flux.
6. Estimated drag coefficients (C_D) were typically relatively large. Despite this, several values were very close to the reference value of 0.0025 for a flat, cohesionless seabed.

5.2 Future research

This research indicates that flux estimates are sensitive to the vertical structure of SSC and velocity, and as such, an array of instruments should be deployed to capture SSC and velocities throughout the full water column. A limitation with most current instrumentation that accurately measures SSC and velocity, is that it becomes difficult to increase resolution past a certain point, due to the size of the instrument and frame

assembly. While there are some OBS arrays that have a relatively high resolution (such as the 1.44 m sensor rod used in Baek et al., (2018)), they are not readily available. Adding more instruments into the water column also increases the chances of confounding the results by altering the flow characteristics of the water column or by inducing turbulence that directly influences sediment resuspension at the bed. As such, methods of measuring full water profiles of velocity and SSC using a single instrument is required to increase the fidelity of flux estimates. In addition, using an array of instruments has other practical problems i.e., the high cost of quality scientific instruments along with the time and resources required to deploy them. Single instruments that can measure either profiles of SSC or velocity do exist, namely acoustic based instruments, i.e., ADCP or ABS. ADCPs are often used to measure currents with high accuracy (MacVean & Lacy, 2014; Mariotti & Fagherazzi, 2012). However, the few studies that have attempted to derive SSC from acoustic instruments in a fine-grained environment have usually had issues with data quality. For example, MacVean & Lacy (2014) calibrated acoustic instruments to measure SSC at 3 sites, and 2 of the 3 calibrations had R^2 values around 0.5. Acoustically derived SSC is difficult to obtain in fine grained environments due to variability in grainsize, the inherent approximations in sonar equations (Mariotti & Fagherazzi, 2012), and processes such as flocculation (Thorne et al., 2014). In order to enable high resolution and accurate measurements of fluxes over the whole water column, we would make several recommendations for areas of future research:

1. Using acoustic backscatter techniques to obtain SSC profiles in fine grained cohesive environments. While this research area remains a long-standing challenge, given the potential benefits for measurements that could arise, efforts should nonetheless continue. In particular, work should be undertaken to explore the relationships between backscattered signal and the concentrations and structure of fine-grained sediments in suspension.
2. Improving the reliability of acoustically derived SSC for various environments compared with existing methods.
3. Increasing the accuracy of fluxes derived from combining acoustic backscatter techniques and current profilers in comparison to more widely used methods. Ultimately the combination of high quality and high-resolution SSC and velocity profiles will allow for significantly more accurate estimates of sediment flux.

References

Andersen, T. J., & Pejrup, M. (2001). Suspended sediment transport on a temperate, microtidal mudflat, the Danish Wadden Sea. *Marine Geology*, *173*(1-4), 69-85.

Baek, Y. S., Chun, S. S., Chang, T. S., & Kim, J. K. (2018). The role of fluid mud in the formation of extensive mud sheets during summer on the Duuri macrotidal flat, west coast of Korea. *Geosciences Journal*, *22*, 19-32.

Bassoullet, P., Le Hir, P., Gouleau, D., & Robert, S. (2000). Sediment transport over an intertidal mudflat: field investigations and estimation of fluxes within the "Baie de Marenngres-Oleron"(France). *Continental Shelf Research*, *20*(12-13), 1635-1653.

Black, K. S. (1999). Suspended sediment dynamics and bed erosion in the high shore mudflat region of the Humber Estuary, UK. *Marine Pollution Bulletin*, *37*(3-7), 122-133.

Christie, M. C., Dyer, K. R., & Turner, P. (1999). Sediment flux and bed level measurements from a macro tidal mudflat. *Estuarine, Coastal and Shelf Science*, *49*(5), 667-688.

Christie, M. C., & Dyer, K. R. (1998). Measurements of the turbid tidal edge over the Skeffling mudflats. *Geological Society, London, Special Publications*, *139*(1), 45-55.

Collins, M. B., Ke, X., & Gao, S. (1998). Tidally-induced flow structure over intertidal flats. *Estuarine, Coastal and Shelf Science*, *46*(2), 233-250.

Colosimo, I., de Vet, P. L., van Maren, D. S., Reniers, A. J., Winterwerp, J. C., & van Prooijen, B. C. (2020). The impact of wind on flow and sediment transport over intertidal flats. *Journal of Marine Science and Engineering*, *8*(11), 910.

Deloffre, J., Lafite, R., Lesueur, P., Lesourd, S., Verney, R., & Guézennec, L. (2005). Sedimentary processes on an intertidal mudflat in the upper macrotidal Seine estuary, France. *Estuarine, Coastal and Shelf Science*, *64*(4), 710-720.

De Boer, W. F. (2007). Seagrass–sediment interactions, positive feedbacks and critical thresholds for occurrence: a review. *Hydrobiologia*, *591*, 5-24.

Dennison, W. C., Orth, R. J., Moore, K. A., Stevenson, J. C., Carter, V., Kollar, S., ... & Batiuk, R. A. (1993). Assessing water quality with submersed aquatic vegetation: habitat requirements as barometers of Chesapeake Bay health. *BioScience*, *43*(2), 86-94.

Dyer, K. R. (1998). The typology of intertidal mudflats. *Geological Society, London, Special Publications*, *139*(1), 11-24.

Dyer, K. R., Christie, M. C., Feates, N., Fennessy, M. J., Pejrup, M., & Van der Lee, W. (2000). An investigation into processes influencing the morphodynamics of an intertidal mudflat, the Dollard Estuary, the Netherlands: I. Hydrodynamics and suspended sediment. *Estuarine, Coastal and Shelf Science*, *50*(5), 607-625.

Eisma, D. (1986). Flocculation and de-flocculation of suspended matter in estuaries. *Netherlands Journal of Sea Research*, *20*(2-3), 183-199.

Fagherazzi, S., Palermo, C., Rulli, M. C., Carniello, L., & Defina, A. (2007). Wind waves in shallow microtidal basins and the dynamic equilibrium of tidal flats. *Journal of Geophysical Research: Earth Surface*, *112*(F2).

Fan, D., Guo, Y., Wang, P., & Shi, J. Z. (2006). Cross-shore variations in morphodynamic processes of an open-coast mudflat in the Changjiang Delta, China: with an emphasis on storm impacts. *Continental Shelf Research*, *26*(4), 517-538.

Fitton, J. M., Hansom, J. D., & Rennie, A. F. (2018). A method for modelling coastal erosion risk: the example of Scotland. *Natural Hazards*, *91*, 931-961.

Floerl, O., Atalah, J., Bugnot, A. B., Chandler, M., Dafforn, K. A., Floerl, L., ... & Major, R. (2021). A global model to forecast coastal hardening and mitigate associated socioecological risks. *Nature Sustainability*, *4*(12), 1060-1067.

Friedrichs, C. T. (2011). Tidal flat morphodynamics: a synthesis.

Friedrichs, C. T., & Aubrey, D. G. (1988). Non-linear tidal distortion in shallow well-mixed estuaries: a synthesis. *Estuarine, Coastal and Shelf Science*, *27*(5), 521-545.

Friedrichs, C. T., & Aubrey, D. G. (1996). Uniform bottom shear stress and equilibrium hyposometry of intertidal flats. *Mixing in Estuaries and Coastal Seas*, *50*, 405-429.

Glade, T. (2003). Landslide occurrence as a response to land use change: a review of evidence from New Zealand. *Catena*, *51*(3-4), 297-314.

Grabowski, R. C., Droppo, I. G., & Wharton, G. (2011). Erodibility of cohesive sediment: The importance of sediment properties. *Earth-Science Reviews*, *105*(3-4), 101-120.

Green, M. O., & Coco, G. (2007). Sediment transport on an estuarine intertidal flat: measurements and conceptual model of waves, rainfall and exchanges with a tidal creek. *Estuarine, Coastal and Shelf Science*, *72*(4), 553-569.

Green, M. O., & Coco, G. (2014). Review of wave-driven sediment resuspension and transport in estuaries. *Reviews of Geophysics*, *52*(1), 77-117.

Green, M. O., Hewitt, J. E., & Thrush, S. F. (1998). Seabed drag coefficient over natural beds of horse mussels (Atrina zelandica). *Journal of Marine Research*, *56*(3), 613-637.

Green, M. O., & MacDonald, I. T. (2001). Processes driving estuary infilling by marine sands on an embayed coast. *Marine Geology*, *178*(1-4), 11-37.

Hall, S. J. (2002). The continental shelf benthic ecosystem: current status, agents for change and future prospects. *Environmental Conservation*, *29*(3), 350-374.

Healy, T. (2002). Chapter Fourteen Muddy coasts of mid-latitude oceanic islands on an active plate margin—New Zealand. In *Proceedings in Marine Science* (Vol. 4, pp. 347-374). Elsevier.

Hicks, D. M., Shankar, U., McKerchar, A. I., Basher, L., Lynn, I., Page, M., & Jessen, M. (2011). Suspended sediment yields from New Zealand rivers. *Journal of Hydrology (New Zealand)*, *50*(1), 81-142.

Horstman, E. M., Lundquist, C. J., Bryan, K. R., Bulmer, R. H., Mullarney, J. C., & Stokes, D. J. (2018). The dynamics of expanding mangroves in New Zealand. *Threats to Mangrove Forests: Hazards, Vulnerability, and Management*, 23-51.

Hughes, A. O., Quinn, J. M., & McKergow, L. A. (2012). Land use influences on suspended sediment yields and event sediment dynamics within two headwater catchments, Waikato, New Zealand. *New Zealand Journal of Marine and Freshwater Research*, *46*(3), 315-333.

Hunt, S., Bryan, K. R., & Mullarney, J. C. (2015). The influence of wind and waves on the existence of stable intertidal morphology in meso-tidal estuaries. *Geomorphology*, *228*, 158-174.

Hunt, S., Bryan, K. R., & Mullarney, J. C. (2017). The effect of wind waves on spring-neap variations in sediment transport in two meso-tidal estuarine basins with contrasting fetch. *Geomorphology*, *280*, 76-88.

Jones, H. F., Hunt, S., Kamke, J., & Townsend, M. (2022). Historical data provides context for recent monitoring and demonstrates 100 years of declining estuarine health. *New Zealand Journal of Marine and Freshwater Research*, *56*(3), 371-388.

Kim, D., Ko, J., Jo, J., Ryu, J., & Choi, K. (2022). Decoupling natural and man-made impacts on the morphologic and sedimentologic changes in the tidal flats, Saemangeum area, west coast of Korea: Implications for benthic ecosystem stability. *Science of The Total Environment*, *807*, 151779.

Kleinhans, M. G., Schuurman, F., Bakx, W., & Markies, H. (2009). Meandering channel dynamics in highly cohesive sediment on an intertidal mud flat in the Westerschelde estuary, the Netherlands. *Geomorphology*, *105*(3-4), 261-276.

Lee, S. C., & Mehta, A. J. (1997). Problems in characterizing dynamics of mud shore profiles. *Journal of Hydraulic Engineering*, *123*(4), 351-361.

Lovett, N. J. (2017). *Sediment transport in the Firth of Thames mangrove forest, New Zealand* (Master of Science (MSc), The University of Waikato, Hamilton, New Zealand; Retrieved from https://hdl.handle.net/10289/11568

MacDonald, I. T., & Mullarney, J. C. (2015). A novel "FlocDrifter" platform for observing flocculation and turbulence processes in a lagrangian frame of reference. *Journal of Atmospheric and Oceanic Technology*, *32*(3), 547-561.

Manning, A. J., Langston, W. J., & Jonas, P. J. C. (2010). A review of sediment dynamics in the Severn Estuary: influence of flocculation. *Marine Pollution Bulletin*, *61*(1-3), 37-51.

Mariotti, G., & Fagherazzi, S. (2012). Channels ‐ tidal flat sediment exchange: The channel spillover mechanism. *Journal of Geophysical Research: Oceans*, *117*(C3).

McDougall, T. J., & Barker, P. M. (2011). Getting started with TEOS-10 and the Gibbs Seawater (GSW) oceanographic toolbox. *Scor/Iapso WG*, *127*(532), 1-28.

MacVean, L. J., & Lacy, J. R. (2014). Interactions between waves, sediment, and turbulence on a shallow estuarine mudflat. *Journal of Geophysical Research: Oceans*, *119*(3), 1534-1553.

Mitchener, H., & Torfs, H. (1996). Erosion of mud/sand mixtures. *Coastal Engineering*, *29*(1-2), 1-25.

Morrison, M. A., Lowe, M. L., Parsons, D. M., Usmar, N. R., & McLeod, I. M. (2009). A review of land-based effects on coastal fisheries and supporting biodiversity in New Zealand. *New Zealand Aquatic Environment and Biodiversity Report*, *37*, 100.

Naish, T. R., Nelson, C. S., & Hodder, A. P. W. (1993). Evolution of Holocene sedimentary bentonite in a shallow-marine embayment, Firth of Thames, New Zealand. *Marine Geology*, *109*(3-4), 267-278.

Nittrouer, C. A., DeMaster, D. J., Eidam, E. F., Nguyen, T. T., Liu, J. P., Ogston, A. S., & Phung, P. V. (2017). The Mekong continental shelf: The primary sink for deltaic sediment particles and their passengers. *Oceanography*, *30*(3), 60-70.

Norkko, A., Thrush, S. F., Hewitt, J. E., Cummings, V. J., Norkko, J., Ellis, J. I., ... & MacDonald, I. (2002). Smothering of estuarine sandflats by terrigenous clay: the role of wind-wave disturbance and bioturbation in site-dependent macrofaunal recovery. *Marine Ecology Progress Series*, *234*, 23-42.

Nowacki, D. J., & Ogston, A. S. (2013). Water and sediment transport of channel-flat systems in a mesotidal mudflat: Willapa Bay, Washington. *Continental Shelf Research*, *60*, S111-S124.

O'brien, D. J., Whitehouse, R. J. S., & Cramp, A. (2000). The cyclic development of a macrotidal mudflat on varying timescales. *Continental Shelf Research*, *20*(12-13), 1593-1619.

Page, M. J., & Trustrum, N. A. (1997). A late Holocene lake sediment record of the erosion response to land use change in a steepland catchment, New Zealand. *Zeitschrift für Geomorphologie*, 369-392.

Ralston, D. K., & Stacey, M. T. (2007). Tidal and meteorological forcing of sediment transport in tributary mudflat channels. *Continental Shelf Research*, *27*(10-11), 1510-1527.

Redder, I. J. (2023). *Using acoustic backscatter data to provide estimates of profiles of suspended sediment concentrations for cohesive particles in the field* (Master of Science (MSc) Research Thesis, The University of Waikato, Hamilton, New Zealand;

Rodil, I. F., Lohrer, A. M., Chiaroni, L. D., Hewitt, J. E., & Thrush, S. F. (2011). Disturbance of sandflats by thin terrigenous sediment deposits: consequences for primary production and nutrient cycling. *Ecological Applications*, *21*(2), 416-426.

Rouse, H. (1937). Modern conceptions of the mechanics of fluid turbulence. *Transactions of the American Society of Civil Engineers*, *102*(1), 463-505.

Shi, B., Yang, S. L., Temmerman, S., Bouma, T., Ysebaert, T., Wang, S., ... & Wang, Y. P. (2021). Effect of typhoon ‐ induced intertidal ‐ flat erosion on dominant macrobenthic species (Meretrix meretrix). *Limnology and Oceanography*, *66*(12), 4197-4209.

Staudt, F., Mullarney, J. C., Pilditch, C. A., & Huhn, K. (2019). Effects of grain-size distribution and shape on sediment bed stability, near-bed flow and bed microstructure. *Earth Surface Processes and Landforms*, *44*(5), 1100-1116.

Styles, R. (2006). Laboratory evaluation of the LISST in a stratified fluid. *Marine Geology*, *227*(1-2), 151-162.

Suif, Z., Yoshimura, C., Saavedra, O., Ahmad, N., & Hul, S. (2017). Suspended sediment dynamics changes in Mekong River basin: possible impacts of dams and climate change. *GEOMATE Journal*, *12*(34), 140-145.

Swales, A., Bentley Sr, S. J., & Lovelock, C. E. (2015). Mangrove-forest evolution in a sediment-rich estuarine system: opportunists or agents of geomorphic change?. *Earth Surface Processes and Landforms*, *40*(12), 1672-1687.

Thorne, P. D., & Hurther, D. (2014). An overview on the use of backscattered sound for measuring suspended particle size and concentration profiles in non-cohesive inorganic sediment transport studies. *Continental Shelf Research*, *73*, 97-118.

Thorne, P. D., MacDonald, I. T., & Vincent, C. E. (2014). Modelling acoustic scattering by suspended flocculating sediments. *Continental Shelf Research*, *88*, 81-91.

Thorne, P. D., Vincent, C. E., Hardcastle, P. J., Rehman, S., & Pearson, N. (1991). Measuring suspended sediment concentrations using acoustic backscatter devices. *Marine Geology*, *98*(1), 7-16.

Thrush, S. F., Hewitt, J. E., Cummings, V. J., Ellis, J. I., Hatton, C., Lohrer, A., & Norkko, A. J. F. I. E. (2004). Muddy waters: elevating sediment input to coastal and estuarine habitats. *Frontiers in Ecology and the Environment*, *2*(6), 299-306.

Trustrum, N. A., Blaschke, P. M., DeRose, R. C., & West, A. W. (1990). Regolith changes and pastoral productivity declines following deforestation in steeplands of North Island, New Zealand. In *Transactions of the 14th International Congress of Soil Science, Kyoto, Japan, August 1990.* (pp. 125-130).

Uncles, R. J., & Stephens, J. A. (2010). Turbidity and sediment transport in a muddy sub-estuary. *Estuarine, Coastal and Shelf Science*, *87*(2), 213-224.

Venancio, K. K., Garcia, P. D., Gireli, T. Z., & CORRêA, T. B. (2020). Hydrodynamic modeling with scenario approach in the evaluation of dredging impacts on coastal erosion in Santos (Brazil). *Ocean & Coastal Management*, *195*, 105227.

Wei, X., Sauvage, S., Le, T. P. Q., Ouillon, S., Orange, D., Vinh, V. D., & Sanchez-Perez, J. M. (2019). A modeling approach to diagnose the impacts of global changes on discharge and suspended sediment concentration within the Red River Basin. *Water*, *11*(5), 958.

Wentworth, C. K. (1922). A scale of grade and class terms for clastic sediments. *The Journal of Geology*, *30*(5), 377-392.

Wheatley, G. (2004). *Applied Numerical Analysis*.

Whitehouse, R. J. S., Bassoullet, P., Dyer, K. R., Mitchener, H. J., & Roberts, W. (2000). The influence of bedforms on flow and sediment transport over intertidal mudflats. *Continental Shelf Research*, *20*(10-11), 1099-1124.

Williams, A. T., Rangel-Buitrago, N., Pranzini, E., & Anfuso, G. (2018). The management of coastal erosion. *Ocean & Coastal Management*, *156*, 4-20.

Woodin, S. A., Wethey, D. S., Hewitt, J. E., & Thrush, S. F. (2012). Small scale terrestrial clay deposits on intertidal sandflats: Behavioral changes and productivity reduction. *Journal of Experimental Marine Biology and Ecology, 413*, 184-191.

Zhang, K., Douglas, B. C., & Leatherman, S. P. (2004). Global warming and coastal erosion. *Climatic Change, 64*, 41-58.

Appendix

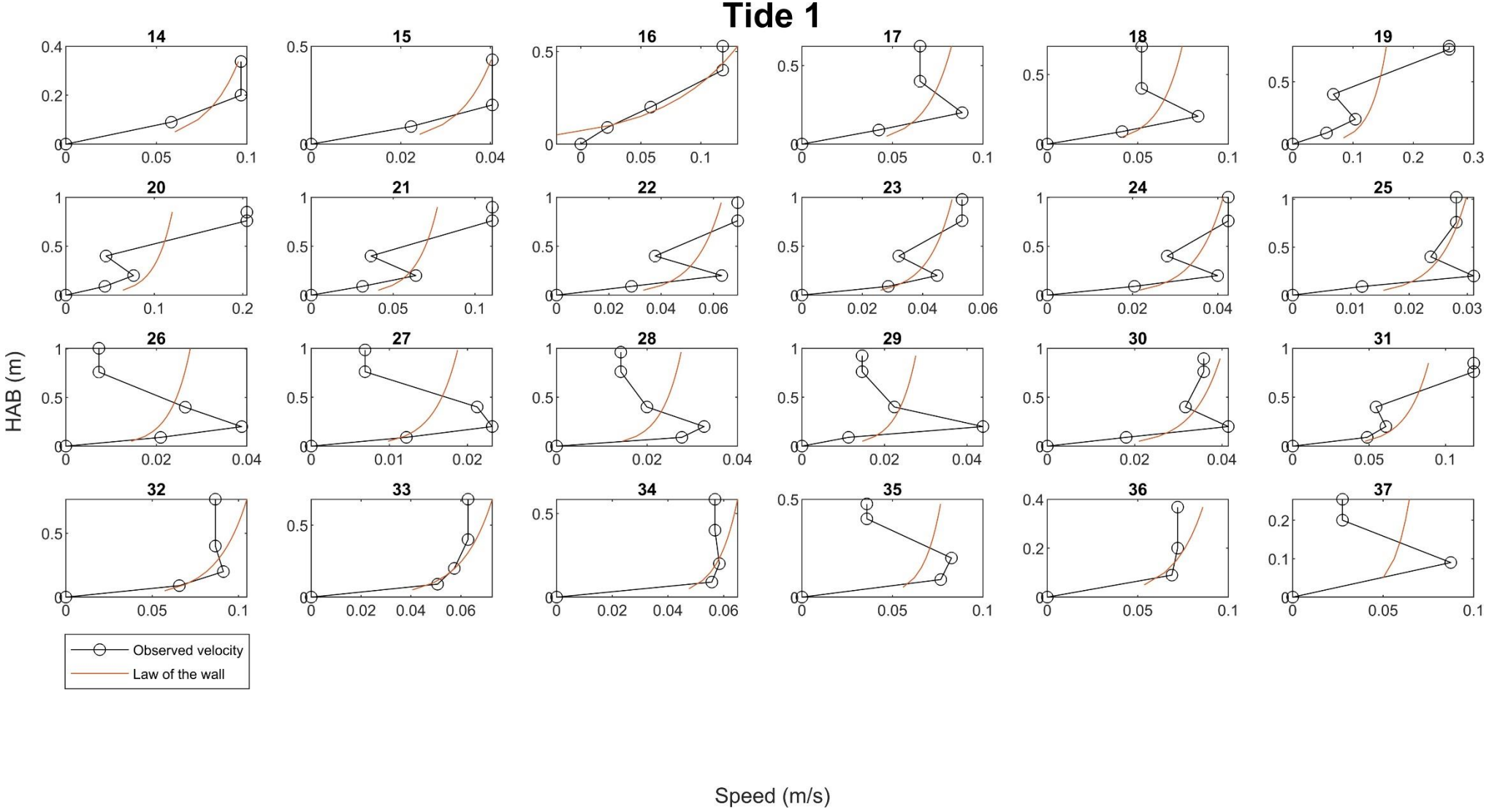

Figure A.1: Measured (with extrapolation Ex1 added) and law of the wall derived speed profiles from the Vectors for each 10-minute burst over tide 1. Numbers above each subplot denote the burst number.

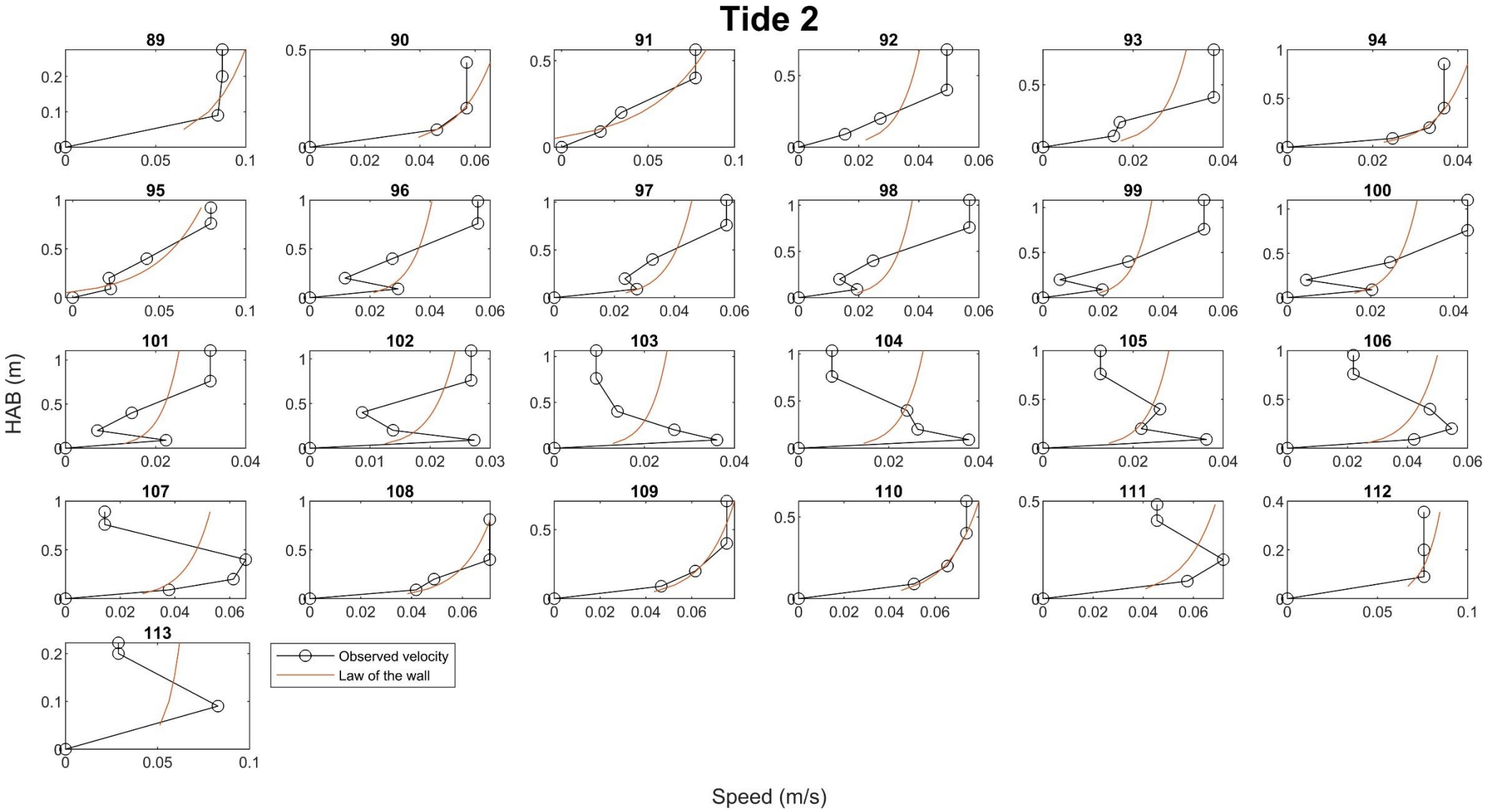

Figure A.2: Measured (with extrapolation Ex1 added) and law of the wall derived speed profiles from the Vectors for each 10-minute burst over tide 2. Numbers above each subplot denote the burst number.

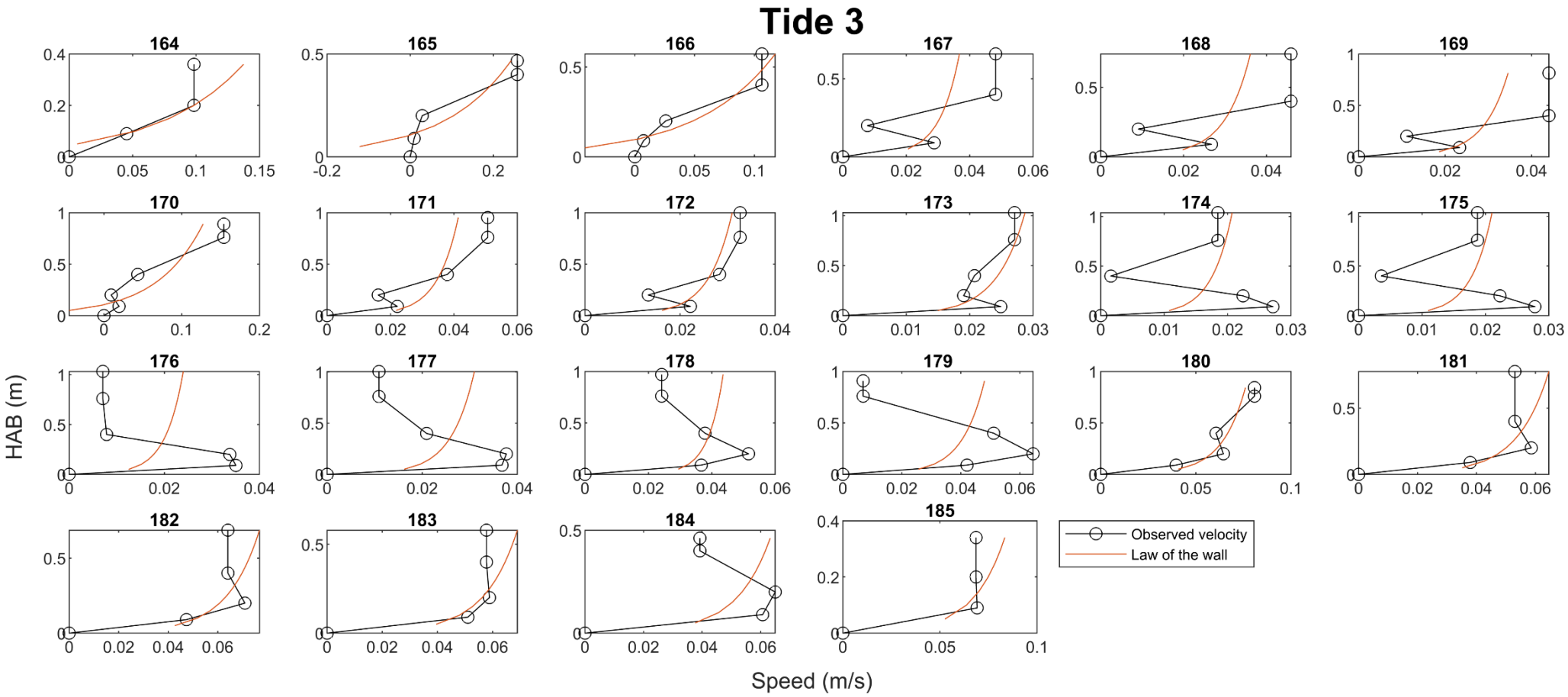

Figure A.3: Measured (with extrapolation Ex1 added) and law of the wall derived speed profiles from the Vectors for each 10-minute burst over tide 3. Numbers above each subplot denote the burst number.

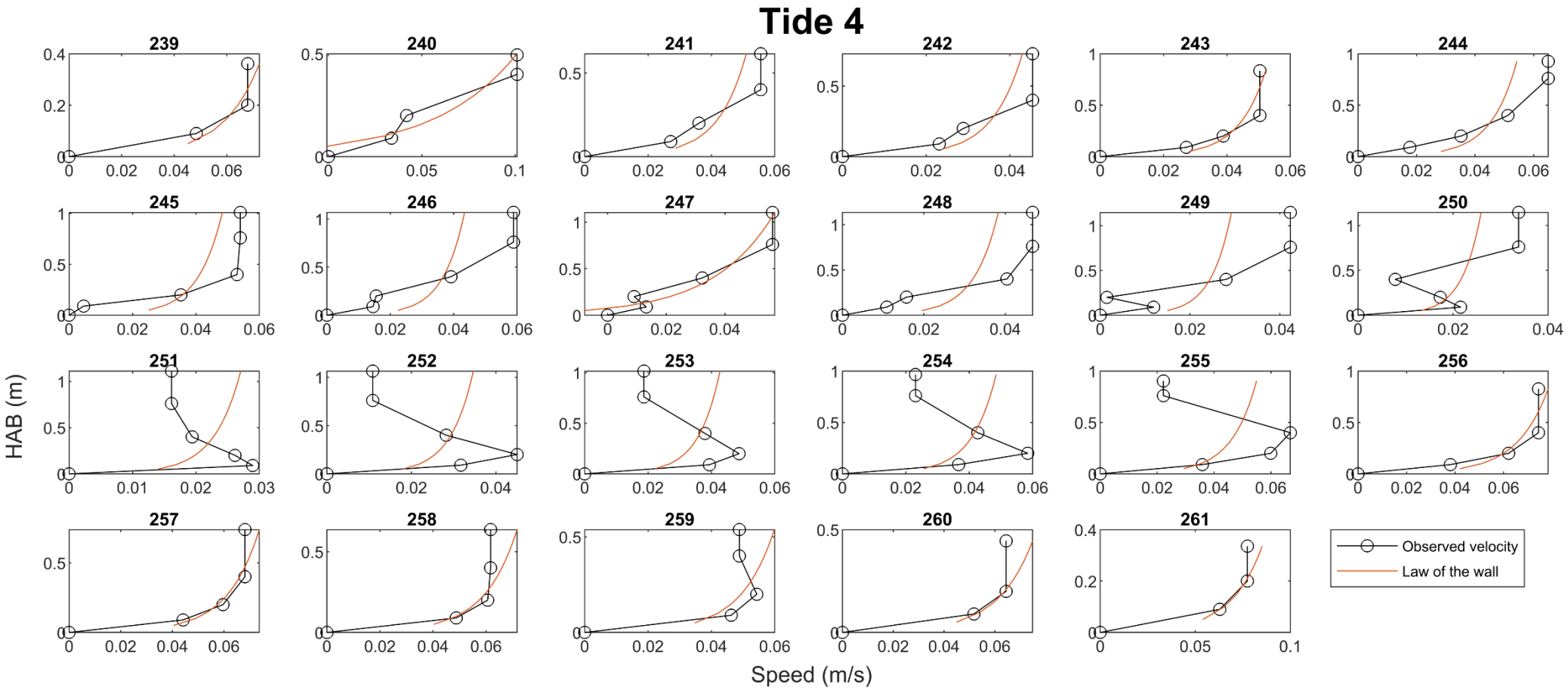

Figure A.4: Measured (with extrapolation Ex1 added) and law of the wall derived speed profiles from the Vectors for each 10-minute burst over tide 4. Numbers above each subplot denote the burst number.

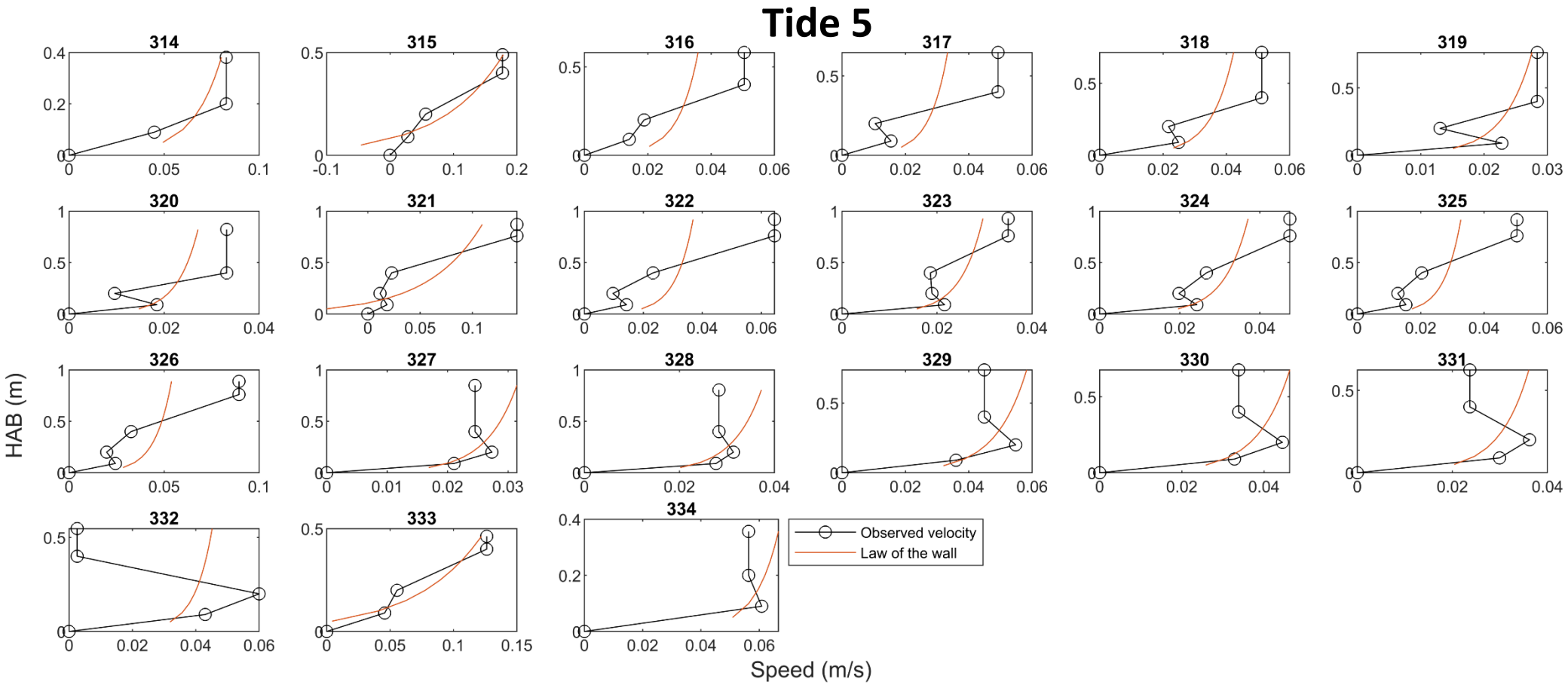

Figure A.5: Measured (with extrapolation Ex1 added) and law of the wall derived speed profiles from the Vectors for each 10-minute burst over tide 5. Numbers above each subplot denote the burst number.

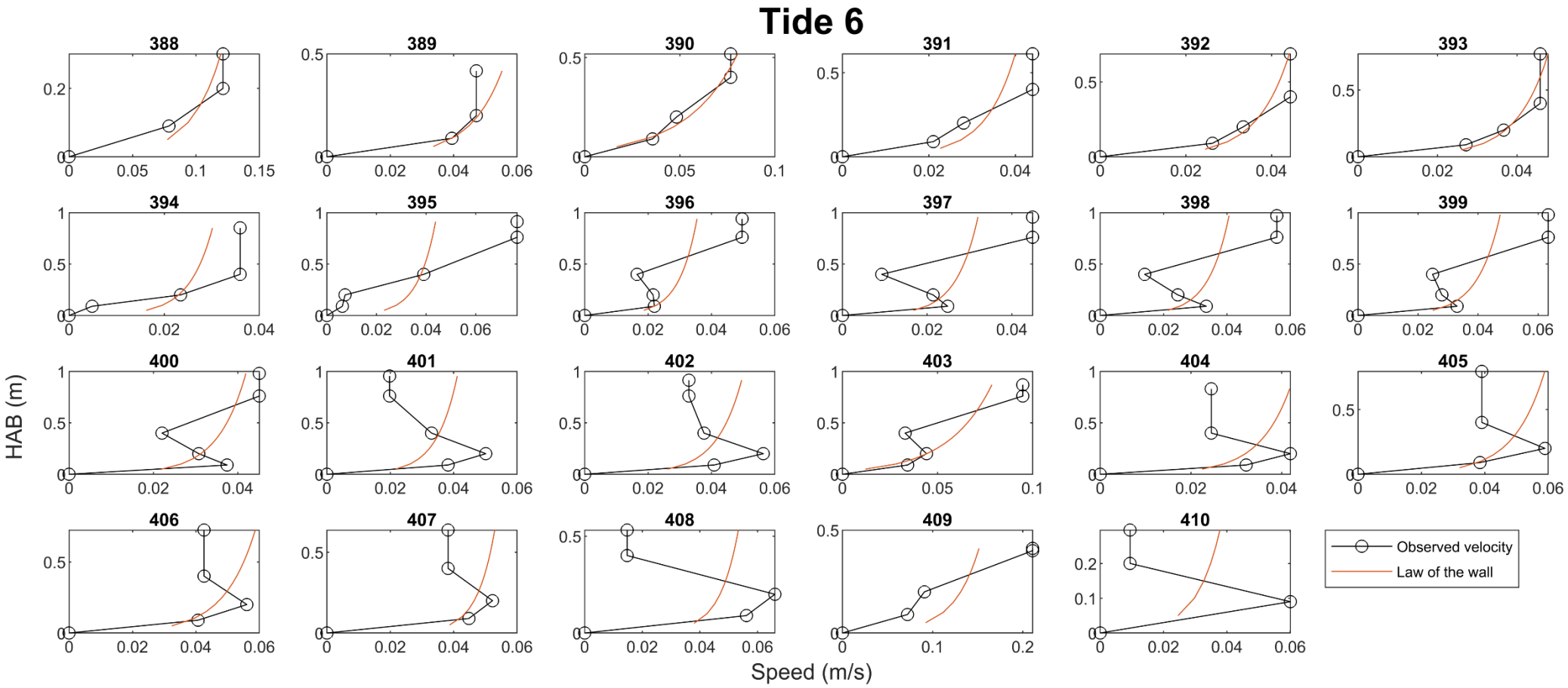

Figure A.6: Measured (with extrapolation Ex1 added) and law of the wall derived speed profiles from the Vectors for each 10-minute burst over tide 6. Numbers above each subplot denote the burst number.

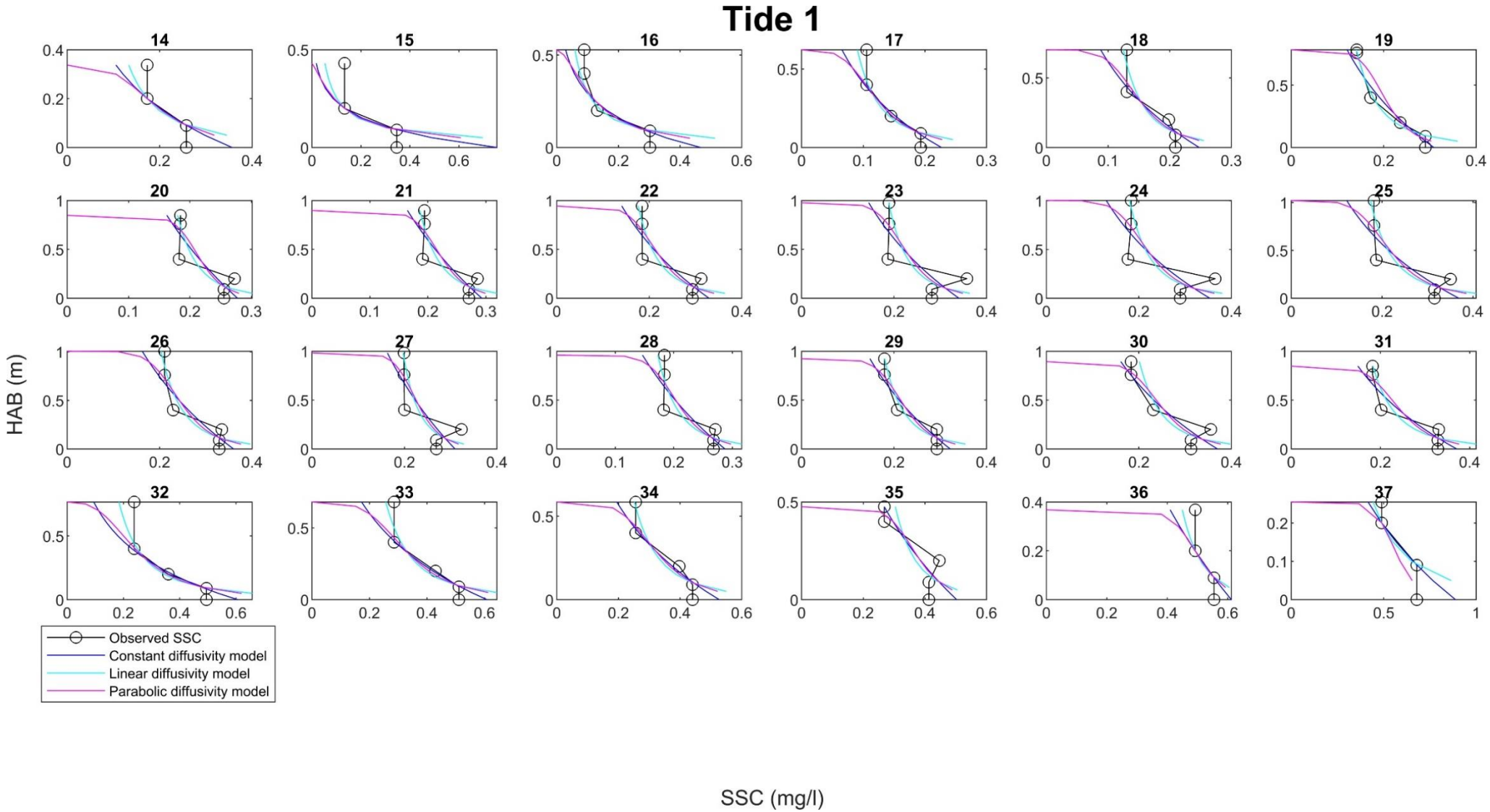

Figure A.7: Measured (with extrapolation Ex1 added) and model derived SSC profiles from the Vectors for each 10-minute burst over tide 1. Numbers above each subplot denote the burst number.

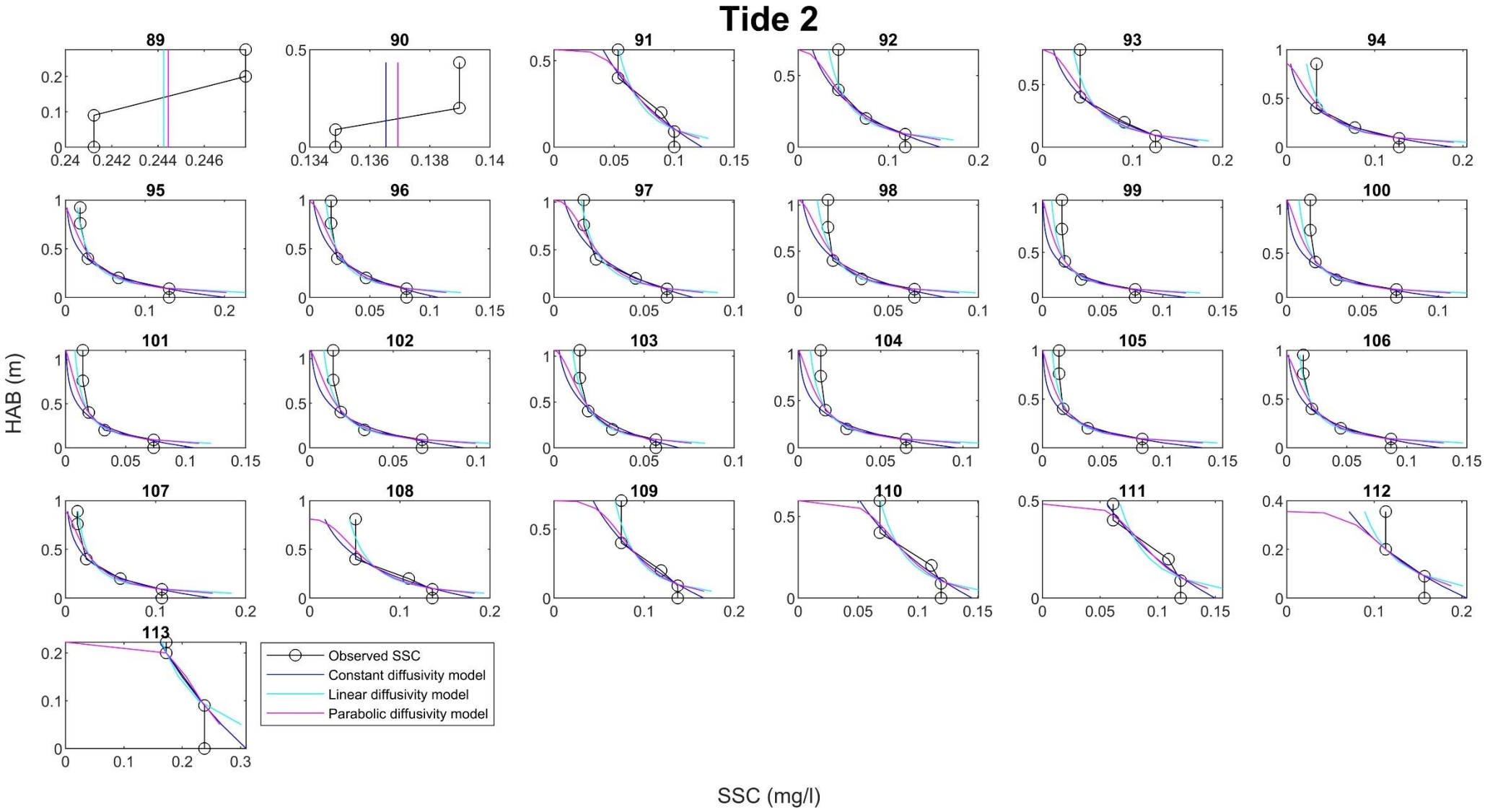

Figure A.8: Measured (with extrapolation Ex1 added) and model derived SSC profiles from the Vectors for each 10-minute burst over tide 2. Numbers above each subplot denote the burst number.

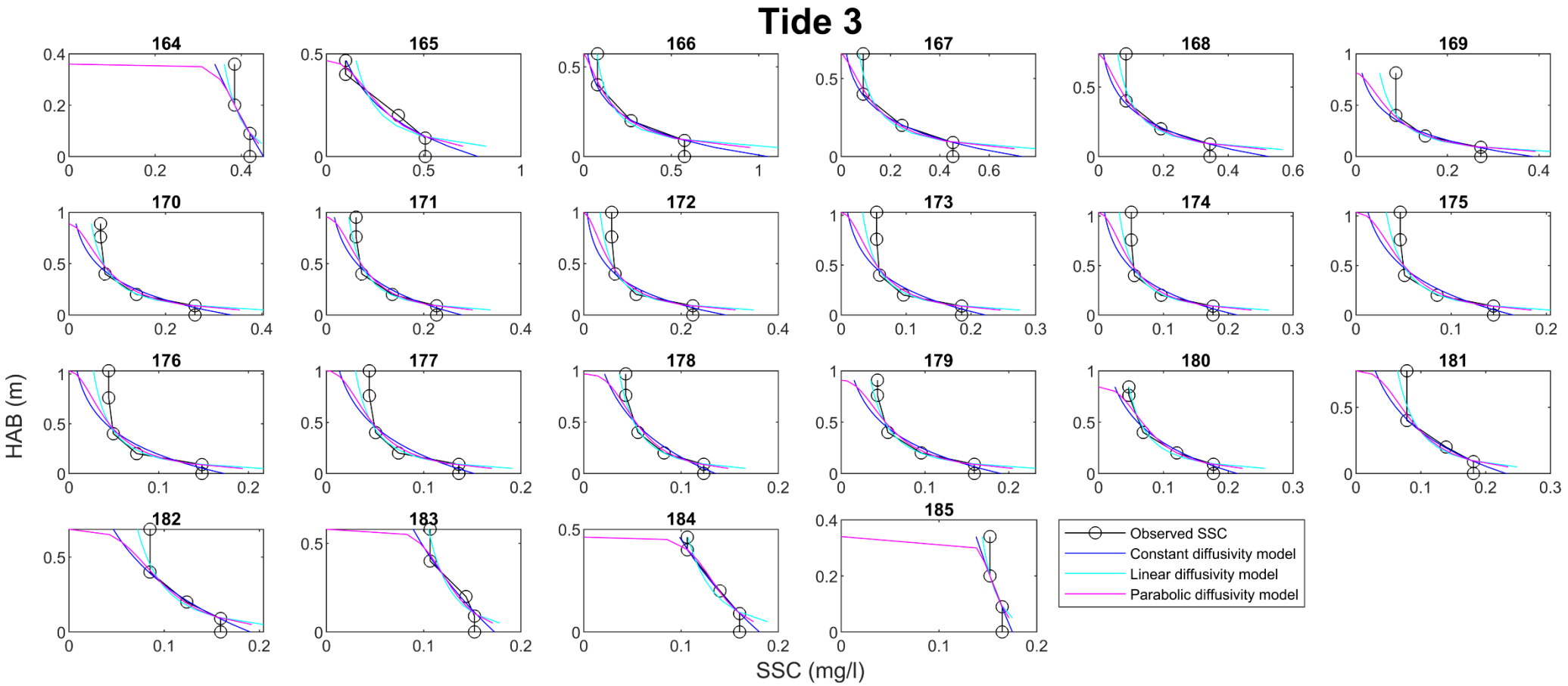

Figure A.9: Measured (with extrapolation Ex1 added) and model derived SSC profiles from the Vectors for each 10-minute burst over tide 3. Numbers above each subplot denote the burst number.

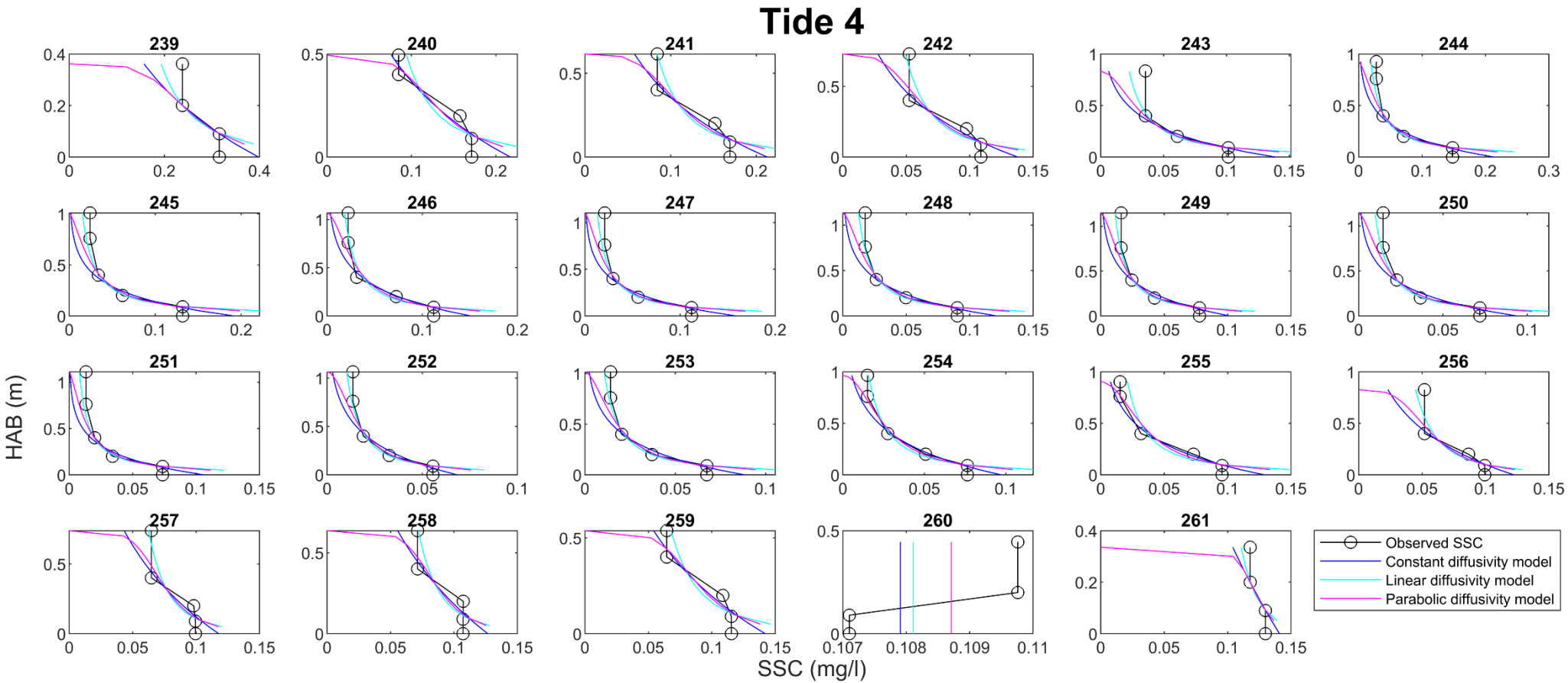

Figure A.10: Measured (with extrapolation Ex1 added) and model derived SSC profiles from the Vectors for each 10-minute burst over tide 4. Numbers above each subplot denote the burst number.

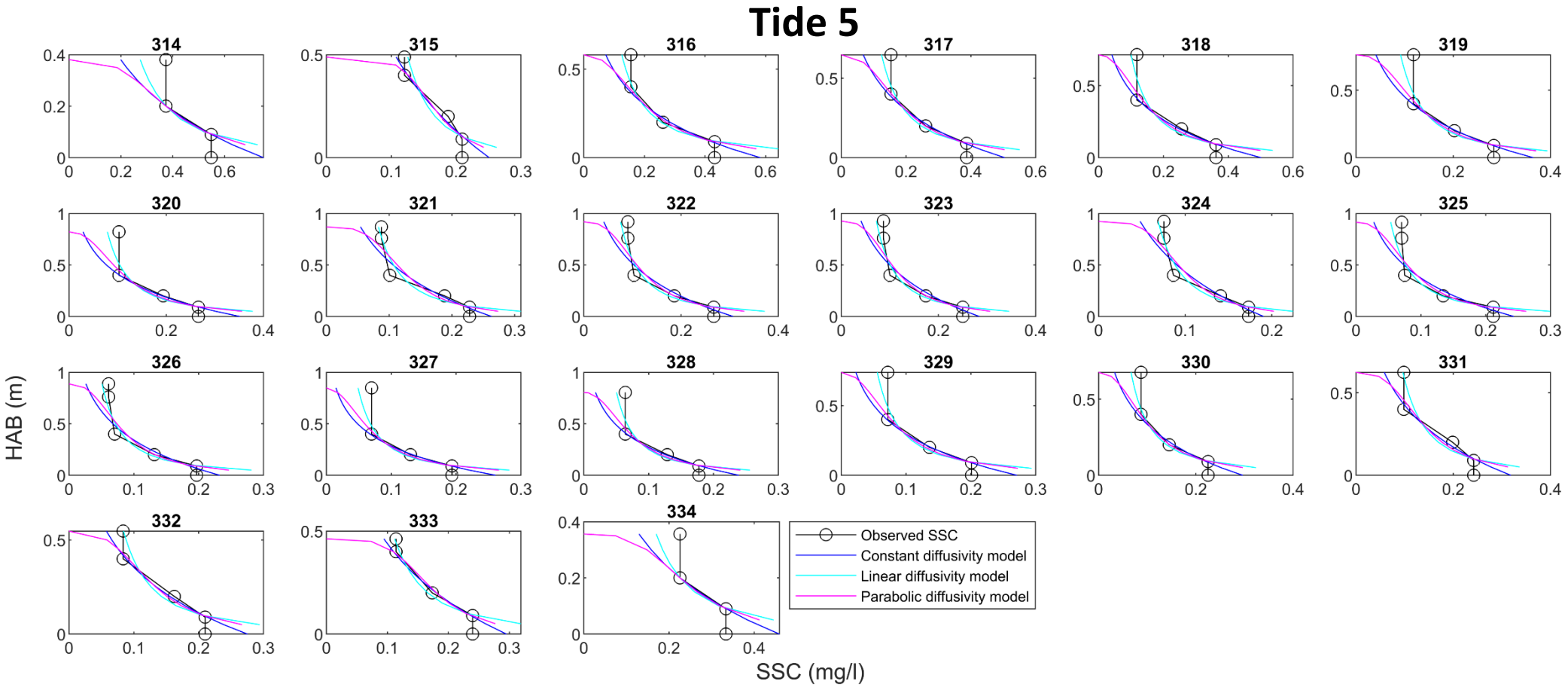

Figure A.11: Measured (with extrapolation Ex1 added) and model derived SSC profiles from the Vectors for each 10-minute burst over tide 5. Numbers above each subplot denote the burst number.

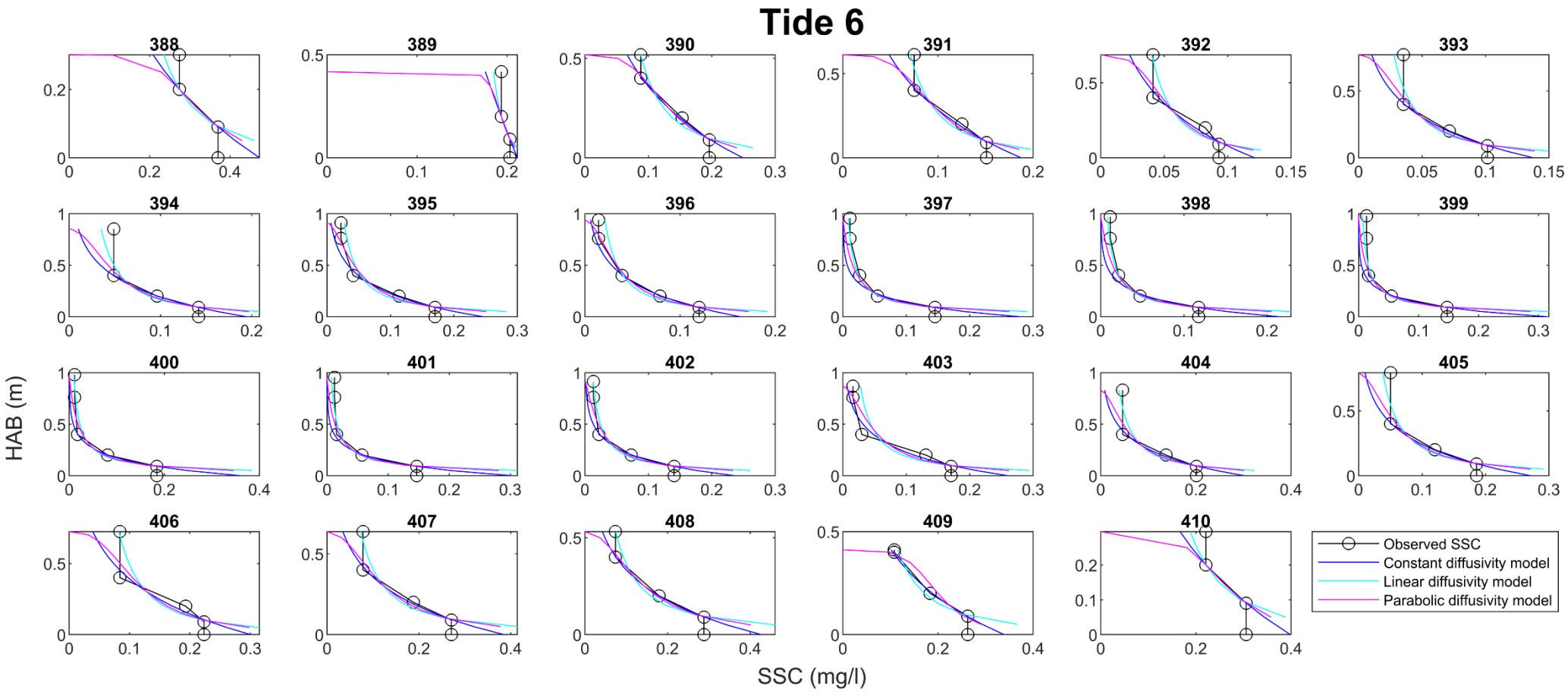

Figure A.12: Measured (with extrapolation Ex1 added) and model derived SSC profiles from the Vectors for each 10-minute burst over tide 6. Numbers above each subplot denote the burst number.